Department of Physics and Astronomy

University of Heidelberg

Master thesis

in Physics

submitted by

Andrea Bergschneider

born in Oberviechtach

2013

Ultracold few-fermion systems

in

multiwell potentials

This Master thesis has been carried out by

Andrea Bergschneider

at the

Physikalisches Institut

under the supervision of

Prof. Dr. Selim Jochim

Ultracold few-fermion systems in multiwell potentials:

This thesis reports on the development and the commissioning of a new setup for the deterministic preparation of ultracold few-fermion systems in a tunable optical potential.

The two key elements of this new setup are a custom-designed high-resolution objective and an acousto-optic deflector (AOD) which are used to create arbitrary potentials with a resolution of $\approx 1\,\mu\mathrm{m}$. Both, the objective and the AOD have been characterized individually in a test setup and combined into a compact setup which was integrated into the existing experiment. With the new setup we observed an improved stability of the preparation of few-particle systems which suggests a decrease of the focus size compared to the old setup. We characterized the new microtrap by measuring its trap frequencies which we found to be consistent with the results obtained in the test setup.

As a first test of the AOD we created a tunable double-well potential and loaded two non-interacting atoms into one of the two wells. By tuning the relative depth of the two wells we could observe resonant tunneling with high contrast and long coherence times. This shows that we can control the created potentials with high accuracy.

Ultrakalte Systeme aus wenigen Fermionen in mehreren Potentialtöpfen:

Diese Arbeit beschreibt Entwicklung und Inbetriebnahme eines neuen Aufbaus zur deterministischen Präparation von ultrakalten Systemen mit wenig Fermionen in einem einstellbaren optischen Potential.

Die beiden Hauptelemente dieses neuen Aufbaus sind ein maßgeschneidertes hochauflösendes Objektiv und ein akusto-optischer Deflektor (AOD), die verwendet werden um beliebige Potentiale mit einer Auflösung von $\approx 1\,\mu\mathrm{m}$ zu erzeugen. Das Objektiv und der AOD wurden jeweils einzeln in einem Versuchsaufbau charakterisiert und dann in einem kompakten Aufbau kombiniert, der in das bestehende Experiment integriert wurde. Mit dem neuen Aufbau erreichten wir eine verbesserte Präparationsstabilität der Wenig-Teilchen-Systeme, was eine verminderte Fokusgröße im Vergleich zum vorherigen Aufbau vermuten lässt. Mit der Messung der Fallenfrequenzen wurde die neue Mikrofalle charakterisiert und es wurden mit dem Testaufbau konsistente Ergebnisse erzielt.

Zum Testen des AODs haben wir ein variables Doppeltopfpotential erzeugt und zwei nicht wechselwirkende Atome in einen der beiden Töpfe geladen. Durch Einstellen der relativen Topftiefen konnten wir resonantes Tunneln mit hohem Kontrast und langer Kohärenzzeit beobachten. Dies zeigt, dass wir die erzeugten Potentiale mit hoher Präzision kontrollieren können.

Contents

Contents

Chapter 1

Introduction

Observing the consequences of quantum statistics requires a system where the inter-particle spacing is comparable to the thermal de Broglie wavelength. For a long time this regime could only be reached in systems of high particle density, until in the last two decades it became possible to cool dilute samples of neutral atoms to low enough temperatures. At these temperatures the description as a Boltzman gas of classical particles breaks down and the behavior of the atoms differs according to their bosonic or fermionic nature. For bosonic systems a phase transition was predicted where the ground state of the system is populated collectively. This so-called Bose-Einstein condensation was first observed in 1995 [Dav95, And95]. For identical fermions collective population of individual states is forbidden due to the Pauli principle. In the limit of zero temperature all available quantum states are filled with one particle per state up to the so-called Fermi energy. For finite temperature this step function is washed out and the occupation probability of the lowest states decreases with increasing temperature according to the Fermi-Dirac distribution. Quantum degeneracy in systems of ultracold fermions was first observed in 1999 [DeM99] where the temperature of the sample was significantly lower than the Fermi energy.

The main advantage of ultracold quantum gases is that their inter-particle interaction is based on simple two-body scattering and can be very well controlled in strength and sign [Ino98]. This makes ultracold gases particularly suited to study many-body systems with strong interactions where theoretical models cannot be restricted to perturbation theory. Hamiltonians which are difficult to solve in theory can be mapped on the many-body Hamiltonian of ultracold gases and studied experimentally. Experiments with quantum gases then act as quantum simulators. One prominent example is the crossover between BEC- and BCS-pairing of fermions. This connection between the limiting cases of a molecular BEC and a BCS-superfluid had been discussed in solid state physics for a long time. However, an experimental realization could not be established until 2004 in ultracold gases [Bar04].

The BCS phase like many other problems in solid state physics has its origin in the interplay between the electron motion and the crystalline structure of solids. For very weak lattice potentials the electrons travel through the crystal nearly unperturbed. For deeper lattice potentials not all energies in the spectrum are allowed for the electrons. These bands in energy are separated by band gaps. If the highest band is partly filled with electrons an applied electric field can cause a net electron transport

and the material is conducting. If the bands are all completely filled the net electron transport is zero. These materials are called band insulators. The stronger the periodic potential gets the narrower the bands become until the electrons are so tightly bound that they are localized primarily on one lattice site.

The structure and filling of the bands gives a valid description of conductivity in a crystalline solid. However, especially for strong periodic potentials the repulsive Coulomb interaction between the electrons with opposite spin can compete with tunneling between the sites. This leads to correlations or even insulation in the system.

A model that describes the competition between the metallic behavior and the Coulomb repulsion sufficiently well is the Hubbard model [Hub63]. It assumes a system of sites filled with spin-up and spin-down electrons. The hopping from one site to the other as well as the interaction between two electrons with different spin occupying the same site are included. In the limit of one single band, there are two well understood cases. If there are two electrons with different spin per site the band is filled and there is no conduction at all. For half-filling, i. e. every site of the system is occupied with one electron in average, the physics depends on the hopping and the strength of the repulsive interaction. If the interaction between the electrons is infinitely large, hopping to adjacent sites is suppressed in the ground state. With the localized electrons this system is in an insulating state although the band is not filled. This state is called a Mott-insulator. If, however, the repulsive interaction between electrons with different spin is large but finite, virtual hopping to adjacent sites can lower the kinetic energy of the system. Due to the Pauli principle the virtual hopping is only possible to sites which are occupied by electrons with opposite spin. Since the delocalization of the electrons lowerst the energy of the system, this effect leads to an anti-ferromagnetic ordering in the lattices.

For any deviation from half-filling the systems get very difficult to solve in theory. Fortunately it turned out that the Hubbard model can be perfectly simulated by ultracold atoms [Jak98]. The periodic structure of the ions in the solid can be mimicked by a periodical optical potential structure into which fermionic atoms are loaded. These optical lattice structures can have different geometries and dimensionalities and with their depth the strength of tunneling can be controlled [Blo05]. The on-site Coulomb interaction is replaced by the contact interaction between fermions with different spins. In contrast to solid state systems this interaction can be tuned in the ultracold atom system. With these two tunable parameters the different phase configurations of the Fermi-Hubbard model can be investigated. Recently, it has even become possible to observe these effects via single-site resolution on the microscopic scale [Bak09, She10].

With optical lattice experiments the predicted fermionic Mott-insulator phase has recently been realized [Jö08, Sch08] and first nearest-neighbor correlations of fermions in a double-well lattice have been shown [Gre13]. The direct observation of long-range anti-ferromagnetic ordering, however, is hampered by the low entropy that is required for long-range order to appear in the system. In fermionic samples evaporative cooling to degeneracy gets inefficient at low temperatures due to Pauli-

blocking and technical noise during the transfer into the lattice potential tends to increase the entropy further. Thus, the currently lowest achievable entropies for a cold fermi gas in a lattice potential are by a factor of two larger than the required transition entropy to end in the anti-ferromagnetically ordered Néel phase [Wer05, Jö10]. Therefore, a lot of effort is currently put into the development of new cooling techniques for quantum gases in optical lattice [McK11].

With our experiment we intend to develop and test a new preparation technique in a well-controlled few-particle system that overcomes this entropy limitation. We are able to prepare number states of fermions in an optical dimple trap in their ground state with a high fidelity [Ser11b]. The fact that in the dimple trap each level up to a distinct energy is occupied with almost 100% probability and all higher levels are empty results in a very low entropy per particle in our single-trap system. If we can extend our system to a few-site potential while keeping the entropy per particle lower than the Néel entropy this should allow us to directly observe anti-ferromagnetic ordering. In this thesis the first step towards this goal was made by the creation and control of a double-well potential.

In chapter 2 the basic theoretical concepts and conditions of anti-ferromagnetic ordering in the Fermi-Hubbard model are introduced and the double-well potential as its simplest realization is presented. Chapter 3 describes our experiment for high-fidelity preparation of a few-fermion system in a single microtrap. It also introduces our established tools for the control and read-out of the few-particle system. The new microtrap setup which provides more flexibility and higher preparation fidelity is described in detail in chapter 4. Here special emphasis is given to the new high-resolution objective and the acousto-optic deflector which allows for the creation of few-site potentials. The implementation and characterization of the new setup as well as the first measurements on a double-well potential are described in chapter 5. In chapter 6 we conclude and give a brief outlook for the next experimental steps towards the observation of magnetic correlations in our system.

Chapter 2

Cold fermions as quantum simulators of the Fermi-Hubbard model

The properties of solid state materials are mostly governed by the behavior of the valence electrons in the material. However, an exact microscopic description of the entire system of electrons including electron-electron interaction, electron-lattice interaction, etc. is very complex and impossible to solve. For nevertheless describing a special effect in condensed matter physics, the problem is simplified by a restriction to the relevant parameters. To explain, e.g., conduction in metals the model of a free electron gas gives a good approximation.

Magnetic ordering in solid state crystals is another issue in condensed matter physics. One of the simplest models to describe electrons that align their spins in a collective way is the Heisenberg model. It assumes the electrons to be pinned on their lattice sites with a spin-spin interaction between the adjacent sites. However, the model of fixed electrons cannot explain the nature of this coupling mechanism.

More realistic descriptions include also hopping of electrons in a periodic lattice potential. Together with the electron-electron interaction this can give rise to collective phenomena in the system. One theoretical model that captures this interplay between hopping and interaction is the Hubbard model [Hub63]. It contains the Heisenberg model as one limit and thus allows to study the mechanism of magnetic ordering and other linked phenomena.

Solving the Hubbard model analytically is only possible in some limits. Recently, it has been suggested to mimic the model by ultracold gases in optical lattices [Jak98]. The periodic potential can be created by optical lattices into which cold fermionic atoms are loaded to simulate the electrons in the solid state. As ultracold gases provide a high level of control over parameters which are predetermined in solid states one hopes to get new insights into this field of physics by using them as quantum simulators.

This chapter will deal with the conceptional steps from magnetism to ultracold gases. Section 2.1 introduces the exchange mechanism that mediates magnetism in crystalline solids. Based on [Yos96] and [McK11] the Fermi-Hubbard models of solid state physics and of ultracold gases are introduced in section 2.2. The different

phases appearing in this kind of systems will be discussed with a special focus on magnetic ordering. In section 2.3 the minimal realization of a finite Fermi-Hubbard system will be discussed, the double-well potential, which will be experimentally feasible with our new setup.

2.1 Mediation of magnetic ordering

The emergence of magnetism is based on collective ordering of the magnetic moments of electrons in a solid due to spin-spin interaction. However, simple magnetic dipolar interaction is much too weak to explain the spin alignment. Instead the interaction is purely based on quantum mechanics that claims anti-symmetrization of the electron wavefunctions and thus leads to an effective spin-spin interaction.

To understand the interaction mechanism that lies at the heart of long-range magnetic order, we consider two electrons located at $\mathbf{r}_1$ and $\mathbf{r}_2$. They interact via Coulomb interaction. To describe the system we choose an ansatz where we take the product of the single wavefunctions to construct the total wavefunction of the system $\Psi(\mathbf{r}_1, \mathbf{r}_2, \mathbf{S}_1, \mathbf{S}_2)$. As the two electrons are indistinguishable the total wavefunction has to be anti-symmetric and obey exchange symmetry. Thus, the two possible eigenfunctions are

$$\Psi_S = \frac{1}{\sqrt{2}}(\psi_\mathrm{a}(\mathbf{r}_1)\psi_\mathrm{b}(\mathbf{r}_2) + \psi_\mathrm{a}(\mathbf{r}_2)\psi_\mathrm{b}(\mathbf{r}_1))\chi_S \quad \text{and} \tag{2.1}$$

$$\Psi_T = \frac{1}{\sqrt{2}}(\psi_\mathrm{a}(\mathbf{r}_1)\psi_\mathrm{b}(\mathbf{r}_2) - \psi_\mathrm{a}(\mathbf{r}_2)\psi_\mathrm{b}(\mathbf{r}_1))\chi_T \tag{2.2}$$

with the anti-symmetric singlet (S=0) spin wavefunction $\chi_S = \frac{1}{\sqrt{2}}(|\uparrow\downarrow\rangle - |\downarrow\uparrow\rangle)$ and the three degenerate symmetric triplet spin wavefunctions χ_T (S=1). The corresponding eigenenergies are given by the singlet eigenenergy E_S and the triplet eigenenergy E_T. In the singlet state, the spins are aligned anti-parallel, whereas in the triplet state they are aligned parallel. So, the energy difference between singlet and triplet state decides the spin alignment of the ground state of the system. This difference depends on the *exchange integral*

$$E_S - E_T = 2 \iint \psi_\mathrm{a}^*(\mathbf{r}_1)\psi_\mathrm{b}^*(\mathbf{r}_2)H\psi_\mathrm{a}(\mathbf{r}_2)\psi_\mathrm{b}(\mathbf{r}_1)\mathrm{d}\mathbf{r}_1\mathrm{d}\mathbf{r}_2 \tag{2.3}$$

with H being the Hamiltonian of the system.

We want to re-write the Hamiltonian of the system in a form that contains only products of the spin functions $\mathbf{S}_1$ and $\mathbf{S}_2$. With the three equal eigenvalues E_T and one eigenvalue E_S it describes the spin alignment and takes the form

$$H_\mathrm{eff} = \frac{1}{4}(E_S + 3E_T) - (E_S - E_T)\mathbf{S}_1 \cdot \mathbf{S}_2 \tag{2.4}$$

$$= const. - 2J\,\mathbf{S}_1 \cdot \mathbf{S}_2 \,. \tag{2.5}$$

where the exchange energy is now represented by a single parameter J. If its value is positive, the spins align in the triplet state; if it is negative, they align in the singlet state.

To describe the many-body behavior in a large system of magnetic moments fixed on lattice sites we extend the two-particle Hamiltonian to the so-called *Heisenberg model*

$$H = -\sum_{ij} J_{ij} \mathbf{S}_i \cdot \mathbf{S}_j \tag{2.6}$$

where we sum over the different lattice sites i, j. In the following we restrict ourselves to interactions between adjacent sites which are described by one parameter J. A positive value of J then correspond to a ferromagnetic alignment, a negative to anti-ferromagnetic ordering. So, the exchange symmetry of the overlapping single-particle wavefunctions causes a long-range alignment of the magnetic moments in the material.

In many transition metals the electrons' wavefunction overlap between the adjacent ions is zero. One prominent example is MnO, where the electrons sit on the Mn^{2+}-ions which are separated by oxygen O^{2-} ions with filled electron shells. In materials with this kind of structure[1] one would not expect magnetic ordering due to a lack of direct exchange. Nevertheless, anti-ferromagnetic ground states are observed. An explanation for this fact was proposed by Kramers [Kra34] assuming an indirect exchange mechanism mediated via the full p-orbital of the ligands in a second order process, the *superexchange*. In MnO the electrons on the manganese ions align such that they are able to virtually hop to the p-orbitals of the oxygen ions. This delocalization parametrized by the hopping parameter t lowers the kinetic energy of the system [And59]. However, two electrons sitting on the same site repel each other with the Coulomb interaction U. This interplay results in an interaction that has the same spin-dependence as expressed in (2.6). In the limit where hopping can be treated as a perturbation the superexchange parameter amounts to $J = -4t^2/U$ and explains the anti-ferromagnetic ordering in the transition-metal salts.

2.2 The Fermi-Hubbard model

For the description of dynamics and phase transitions in a solid a model like the Heisenberg model with fixed electrons is not suited. A more general model Hamiltonian is necessary that has the Heisenberg model as a limit but also contains tunneling and on-site interaction of the electrons to explain electron correlation effects like superconductivity or magnetic phases.

In general the Hamiltonian describing motion and interaction of the electrons in a lattice can be parametrized as

$$H = H_{\text{crystal}} + H_{\text{int}} \tag{2.7}$$

---

[1] The insulating material La_2CuO_4 [Aha88] being the basis for the high-temperature superconducting $La_{2-x}(Sr,Ba)_xCuO_{4-y}$ also shows this kind of structure and exhibits anti-ferromagnetic ordering.

where the one-body Hamiltonian H_{crystal} contains the kinetic energy of the electrons and the periodic potential and H_{int} describes the Coulomb interaction between two electrons.

The limit of deep periodic potentials where the electrons are primarily localized around the ion positions is of special interest. It is thus suitable to describe the system in the Wannier basis $w_i(\mathbf{r})$ which is a complete orthogonal eigenbasis in position space reflecting the localization around the sites i. We further restrict ourselves to tunneling of the electrons between adjacent sites and interaction between electrons occupying the same site. This is justified by the deep lattice and the screened Coulomb potential of the electrons due to underlying closed electron shells [Ima98]. In addition, the relevant energy scales shall be small compared to the excitation energy required to lift electrons into the next higher band of the lattice potential.

For a homogeneous system the single electron tunneling rate t and the on-site interaction energy U between two electrons with opposite spin can be written in the Wannier basis as

$$t = \int w_i^*(\mathbf{r})\, H_{\text{crystal}}\, w_j(\mathbf{r})\mathrm{d}\mathbf{r} \quad \text{and} \tag{2.8}$$

$$U = \iint |w_i(\mathbf{r}_1)|^2 H_{\text{int}} |w_i(\mathbf{r}_2)|^2 \mathrm{d}\mathbf{r}_1 \mathrm{d}\mathbf{r}_2\,. \tag{2.9}$$

Using the two parameters the system's Hamiltonian can be rewritten in second quantization

$$H = -t \sum_{\sigma,\langle i,j\rangle} a_{i\sigma}^\dagger a_{j\sigma} + U \sum_j n_{j\downarrow}n_{j\uparrow} \quad. \tag{2.10}$$

with $\langle i,j \rangle$ denoting the summation over adjacent sites. The creation (annihilation) operator $a_{i\sigma}^\dagger$ ($a_{i\sigma}$) for both spin components $\sigma =\uparrow,\downarrow$ obey the fermionic anti-commutation relation and $n_{i,\sigma} = a_{i\sigma}^\dagger a_{i\sigma}$ is the occupation number operator. (2.10) is called the Hubbard Hamiltonian. The first term expresses the kinetic energy, the second term the Coulomb interaction of the system.

The relative sizes of the two terms describe the physics of the system. For vanishing on-site interaction (2.10) becomes a single-particle Hamiltonian with the movement of the conduction electrons in the crystal described by Bloch waves. In the limit of $t \gg U$, the interaction can be treated as perturbation. The electrons move around the whole crystal but the states where two electrons sit on one site are suppressed which leads to strong correlations.

For an increase of the ratio U/t in a half-filled lattice, i.e. one electron per lattice site, the Hubbard model predicts a phase transition from a conducting state to an insulating state where the electrons tend to be localized on the lattice sites due to the strong on-site interaction. This phase is called a *Mott insulator*. Note that it contains no spin alignment.

In the limit of large interaction $U \to \infty$ the tunneling can be treated as perturbation.

For half filling, the Hamiltonian can be reduced to the Heisenberg Hamiltonian [Yos96]

$$H_{\text{Heisenberg}} \propto \frac{4\,t^2}{U} \sum_{\langle i,j \rangle} \mathbf{S}_i \cdot \mathbf{S}_j \,. \tag{2.11}$$

In this limit we expect anti-ferromagnetic ordering at low enough temperatures due to the superexchange (cf. section 2.1). If the first term in the Hubbard Hamiltonian vanishes completely the electrons are localized at the lattices sites and neither tunneling nor ordering occurs.

The fact that tunneling and interaction in a lattice are described by only two parameters makes the Hubbard model very simple. Nevertheless, it is not analytically solvable except for the mentioned limiting cases $t \gg U$ and $U \gg t$ in a half-filling configuration. Due to the sheer size of the system the computational analysis of the Hubbard model is still a topic of ongoing investigations.

2.2.1 The Fermi-Hubbard model of ultracold gases

In 1998 it has been pointed out by Jaksch et al. [Jak98] that ultracold atoms in a lattice can simulate the Hubbard model. The electrons are mimicked by two hyperfine components of cold fermionic atoms and the ionic crystal is simulated by an optical lattice creating a periodic potential. This leads to the Fermi-Hubbard Hamiltonian with similar form as in equation $(2.10)^2$ with the corresponding tunneling and on-site interaction parameters

$$t = \int w_i^*(\mathbf{r}) \left[-\frac{\hbar^2}{2m} \nabla^2 + V(\mathbf{r}) \right] w_j(\mathbf{r}) \mathrm{d}\mathbf{r} \quad \text{and} \tag{2.12}$$

$$U = V_{\text{int}} \int |w(\mathbf{r})|^4 \mathrm{d}\mathbf{r} \,. \tag{2.13}$$

$V(\mathbf{r})$ is the periodic potential of the optical lattice that has a often sinusoidal form. In contrast to the long-range Coulomb interaction between electrons, ultracold fermionic atoms in different hyperfine states interact via s-wave collisions. This short-range interaction depends on the scattering length a (cf. section 3.1.3) and has a strength of $V_{\text{int}} = \frac{4\pi\hbar^2 a}{m}$, with m being the atomic mass.

With the help of the optical lattice depth and the scattering length, the Hubbard parameters can be tuned nearly arbitrarily. The tunneling is decreased by increasing the lattice depth. In addition, the on-site interaction can be tuned by changing the scattering length a via magnetic Feshbach resonances.

The tunability of the system led to the observation of the transition between superfluid and Mott insulating state [Jö08, Sch08] for increasing repulsive on-site

---

[2]Note that in optical lattices there exists an overall potential. It alters the depths of the different lattice sites and therefore one actually has to add an addition term $\sum_i \mu_i(n_{i,\uparrow} + n_{i,\downarrow})$. In the system presented in this thesis, however, the depth of the potential wells can be tuned such that they are equally deep. Thus, the additional term does not have a spatial dependency and can be omitted.

interaction. This phase transition is predicted to be at $U/t = 5.8\,z$ with z the number of nearest neighbors in the system [Jak98]. The experimental realization of the Mott insulator phase impressively illustrated the applicability of ultracold atoms as a quantum simulator for condensed matter systems described by the Hubbard Hamiltonian.

2.2.2 Entering the Néel phase

In spite of the demonstration of the superfluid-to-Mott insulator transition in an optical lattice the anti-ferromagnetically ordered phase has not been observed yet. The reason for this is the low transition temperature, the so-called Néel temperature T_N that is necessary to enter the anti-ferromagnetic state. In the limit of the Heisenberg model, i.e. U/t very large, this temperature is on the order[3] of the superexchange energy $T_N \propto 4t^2/U$. Below, anti-ferromagnetic ordering manifests itself as an alternating alignment of spin-up and spin-down states, denoted as Néel phase.

From the point of view of statistical physics, it is not sufficient just to reduce the temperature of the system. The more important criterion for entering into an ordered phase is the entropy per particle. We want to estimate an upper boundary for the entropy of the system by determining the entropy of a non-ordered state. We assume a temperature of $T = 0$ and no particle-hole excitations. Our homogeneous system has N sites that we want to fill with N particles with either spin-up or spin-down. This results in $\Omega = 2^N$ possible combinations representing a completely non-ordered state. The entropy per particle s of that state is then

$$s = S/N = k_{\mathrm{B}}\ln(\Omega)/N = k_{\mathrm{B}}\ln(2) \approx 0.7 k_{\mathrm{B}}\,. \tag{2.14}$$

The critical entropy per particle s_{N} to enter the Néel phase can be calculated by a mean field theory of the three dimensional Heisenberg model which gives the same result. However quantum fluctuations reduce the expected entropy to enter into the Néel phase by a factor of two [Wer05, DL08, Koe08] such that we can assume $s_{\mathrm{N}}/k_{\mathrm{B}} \approx 0.5\ln(2)$.

Entering this regime would allow for the observation and investigation of the transition to the anti-ferromagnetic phase as a function of U/t. Still, current lattice experiments are unable to prepare systems with lower entropies than $s = 0.7\,k_{\mathrm{B}}$ [Jö10]. The limitation is the ineffective cooling of fermions to low temperatures before loading them into the lattice. Therefore many new cooling techniques have been proposed to access this entropy regime [McK11].

In our experiment we try to pursue another strategy. We established a technique (cf. section 4) to deterministically prepare ground-state systems of a specific number of atoms in a single-well potential. In about 90% of the realizations, our system has the desired atom number and is in the ground state which has an entropy per

---

[3]The exact prefactor depends on the lattice and amounts to 0.957 for a cubic lattice [Sta00]

particle of $s = 0$. In the remaining 10% of our realizations the atom number is not as desired.

We can estimate the entropy S of our system by taking into account all the possible preparations that are not the desired state. For this, we use the Shannon entropy which quantifies information in a system. We sum up the probabilities p_i of all the different states i in which the system ends for a distinct number preparation

$$S = -\sum_i p_i \log_2(p_i).$$ (2.15)

For the calculation of the entropy we assumed that the probability for excitations in our system is negligible and that realizations which only differ by their spin have equal probability. For the preparation fidelities measured in [Ser11b] this yields an entropy per particle of $s\,(n=2) \approx 0.24$ and $s\,(n=8) \approx 0.11$ with n the intended number of prepared atoms. However, one should note that the Shannon entropy of our system cannot be directly compared to the critical entopy for anti-ferromagnetic order and is therefore only meant as a rough estimate.

The observation of anti-ferromagnetic order would be possible in our system if atoms could be prepared in multiple wells with low enough entropies. An even higher initial preparation fidelity will further faciliate this project. A new high-resolution objective to increase the preparation fidelity has been implemented in the course of this thesis. It will be presented in section 5.1. The setup to create multiple-well potentials will be presented in section 4.3.

In order to gain experience with the system of multiple wells and explore its capabilities, we start with a double-well potential which can already be described by the Fermi-Hubbard model. The control scheme, the preparations of atoms in this potential and first tunneling measurements (cf. section 5.3) were also part of this thesis.

2.3 The double-well potential

Magnetic correlations as presented in section 2.1 can already be explained with a two-particle system. For their observation two sites are sufficient, as demonstrated in a lattice of double wells in [Gre13]. These double-well potentials are generated by superimposing two optical lattices with different lattice periodicity. By tuning the power in the lattice beams or the scattering length the tunneling and the on-site interaction energy can be set.

In our experiment we can create an isolated double-well potential by two focused Gaussian beams that are partially overlapping (cf. figure 2.1). The potential form is proportional to the intensity distribution of the two superimposed Gaussians. The Hubbard parameter t can be tuned by altering the separation of the wells d, their relative depth $\delta = |I_1 - I_2|$ and the total depth P_{tot} as this changes the overlap and the form of the wavefunctions in the two wells. Additionally we can tune the interaction parameter U by changing the scattering length of the particles.
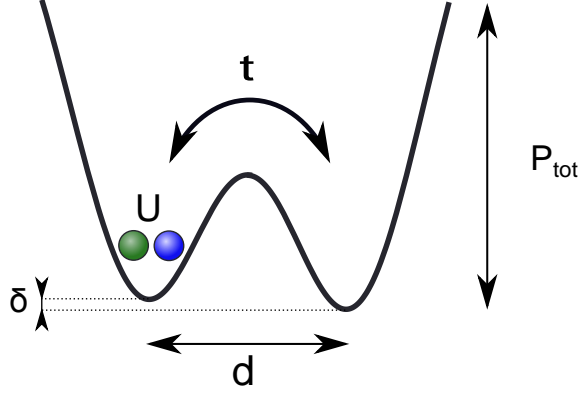
Figure 2.1: Double-well potential with tunable control parameters. With our experimental setup we can tune the total depth P_{tot} of the potential and the separation of the wells d as well as their individual depths. Thus the potential tilt δ, the tunneling rate t and the on-site interaction U can be tuned. Note that U can also be tuned by the changing the inter-particle scattering length.

To calculate the parameters of our double-well system, we reduce the three-dimensional potential to a symmetric double well in one dimension (1D) along the connection of the two wells and solve it numerically. This calculation has been performed by V. Klinkhamer [Kli12] using a reduced potential of the form

$$V(x, d, \delta) \propto \frac{2P_{\text{tot}}}{\pi w_0^2} \left(\exp\left[-2 \frac{(x + \frac{d}{2})^2}{w_0^2} \right] + \exp\left[-2 \frac{(x - \frac{d}{2})^2}{w_0^2} \right] \right) \tag{2.16}$$

where w_0 is the beam waist at the focus and d is the distance of the wells.

For equal depth the two lowest lying eigenstates in the double-well potential are the anti-symmetric and symmetric superposition of the lowest states on the left and the right sites $\Psi_{\text{S,A}} = (\Psi_{\text{L}} \pm \Psi_{\text{R}})/\sqrt{2}$. The eigenenergies are denoted as $E_{\text{S,A}}$ with $E_{\text{S}} \leq E_{\text{A}}$. The energies of the left-sited Ψ_{L} and the right-sited Ψ_{R} are equal. Suppose we start with an atom sitting on the left site, it is in a superposition of the two eigenstates Ψ_{S} and Ψ_{A}. It will oscillate to the right site and back with an oscillation frequency that is given by the energy difference between the two eigenstates $\Omega = \langle \Psi_{\text{L}} | H | \Psi_{\text{R}} \rangle / 2\hbar = (E_S - E_A)/\hbar$. This corresponds to twice the tunneling parameter t described in equation 2.13. The oscillation frequency can be changed by altering the well separation d or the total potential depth P_{tot}.

Figure 2.2 a shows the results of the 1D calculation [Kli12] for the tunneling rate as a function of the well separation. We used the experimentally achievable parameters of a focus waist of $1.15\,\mu\text{m}$ and a total power in the beams of $100\,\mu\text{W}$. With increasing separation of the two wells the tunneling rate decreases. For a fixed separation of $2.16\,\mu\text{m}$ the tunneling rate as a function of the total power is shown in Figure 2.2 b. For increasing trap depth, the wave function gets more localized which leads to a decrease of the tunneling rate. So, by changing the power by one order of magnitude we can tune the tunneling rate by three orders of magnitude. This
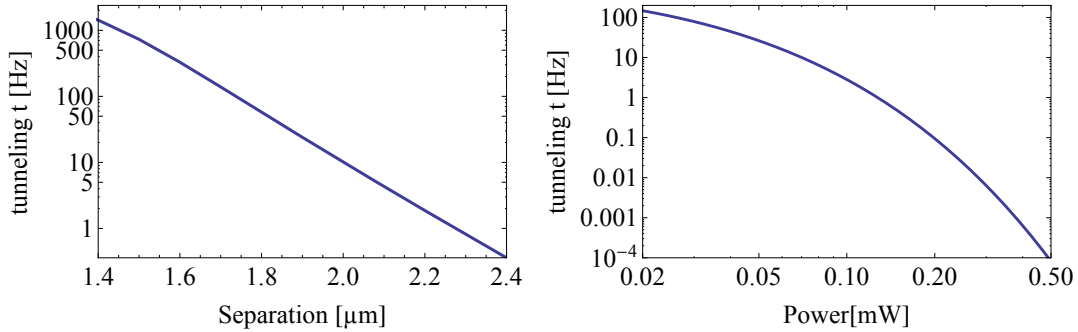
Figure 2.2: Tunability of the tunneling rate for experimentally achievable parameters. (left) shows the tunneling rate at a total power of $100\,\mu\mathrm{W}$ as a function of the well separation. (right) depicts the tunneling rate t for a well separation of $2.16\,\mu\mathrm{m}$ as a function of the total power in the potential. For growing well separation and total power the tunneling decreases.

enables us to switch the tunneling on and off as the accessible measurement time scales in our system are reaching from $500\,\mathrm{Hz}$ to $5\,\mathrm{Hz}$ and slower tunneling rates are not detectable.

If the two sites are not equally deep, the energies of the states Ψ_L and Ψ_R are not equal anymore. This can be regarded as a detuning Δ to the transition. It diminishes the oscillation amplitude and increases the oscillation frequency. We describe the oscillation in the two-level system according to

$$P_R(t) = \langle \Psi(t)|\Psi_R\rangle = \frac{\Omega^2}{\Omega^2 + \Delta^2} \sin^2\left(\frac{\sqrt{\Omega^2 + \Delta^2}\,t}{2}\right) \quad , \qquad (2.17)$$

The maximization of the oscillation amplitude can be used to set the two wells to equal depth in the experiment as we will show in section 5.3.2.

Without any interaction in the system, two fermions with different spins will tunnel back and forth in the double-well potential independently. By tuning the scattering length a to finite values the inter-particle interaction strength U can be tuned between attraction and repulsion. This will lead either to correlated pair tunneling or to anti-correlation like in a Mott insulator, respectively.

2.3.1 Observation of the superexchange

With the two tunable Hubbard parameters t and U we are able to investigate Fermi-Hubbard physics in a double-well potential. We intend to observe superexchange oscillations as already demonstrated in [Tro08, Gre13]. For its observation the superexchange parameter $J = -4t^2/U$ has to be at accessible time scales in our system, i. e larger than $\approx 10\,\mathrm{Hz}$.

To investigate the superexchange mechanism we have to prepare a system in the limit of tight binding, where the Fermi-Hubbard model is valid. This means that the

lattice is deep enough such that in the lowest energy band the atoms are located on the lattice sites and can only tunnel to adjacent sites. In optical lattices the tight-binding limit is described by the parameter V_0/E_R where V_0 is the lattice depth and E_R is the recoil energy. The recoil energy in a lattice of counter-propagating beams is

$$E_R = \frac{h^2}{2m\lambda^2} \tag{2.18}$$

where λ is the wavelength of the trap light used for the standing-wave lattice, m is the atom mass and h is Planck's constant. If $V_0/E_R > 5$ the tight-binding limit is fulfilled [Sch10].

To estimate the effective lattice depth in our double-well potential we use the distance of the two minima to calculate E_R. The lattice depth V_0 is then the energy of the barrier height between the two sites. The tight-binding limit gives constrains on the tunneling rate t which depends on the well separation d and the total power P_{tot} in the trap. By tuning the two parameters appropriately we can almost in any case fulfill the tight-binding requirement.

By tuning the repulsive inter-particle interaction, we want to access the Mott-insulator regime, where hopping of atoms between the adjacent sites is suppressed and only the virtual hopping of the superexchange takes place. This regime is entered for $U/t = 5.8\,z$ [Jak98] where z is the number of neighboring sites in the lattice. To investigate the phase diagram we intend to measure the superexchange at different U/t in the Mott-insulator regime.

For maximizing the superexchange parameter, we can in principle choose a high tunneling rate and increase the interaction such that, U/t stays constant. So, the maximum frequency of the superexchange oscillation is only proportional to the interaction U. However, as we want to stay in the limit of weak interaction, U has to be a lot smaller than the energy level spacing $\hbar\omega$ in the trapping potential. This sets a constraint on the potential depth. Suppose trap frequencies of about 10 kHz and an interaction energy of at most 20% of the trap frequency. Then the observable superexchange oscillation deep in the Mott-insulator regime ($U/t = 20$) has a frequency of $J = \frac{4U}{(U/t)^2} \approx 20$ Hz. Around the phase transition $U/t = 6$ the superexchange constant amounts to $J \approx 220$ Hz. This estimation shows the accessibility of the relevant timescales in our experimental setup.

We expect the Hubbard parameters t and U in the three-dimensional double well to differ from the 1D-calculations. However, they should be on the same order of magnitude and provide the same tunability range, such that we can access the interesting regimes with our experimental setup. After the investigation of the double well a next step will be the extension to more wells where anti-ferromagnetism with long-range order should be present.

Chapter 3

Our system for high-fidelity preparation of small atom numbers

In the previous chapter we explained that a system with low entropy per particle is required to observe anti-ferromagnetic ordering of fermions. Up to now such low entropies cannot be achieved in lattice experiments. In our setup we follow the approach of loading fermions at quantum degeneracy into one single potential well and subsequently spilling it to the desired atom number with a high fidelity. Thus we achieve a few-particle system in its ground state with a high probability. This is equivalent to a low entropy per particle in the system.

Our technique of high-fidelity preparation will be presented in the following chapter. In our apparatus we cool a large sample of fermionic lithium down to quantum degeneracy by using the common cooling techniques, presented in section 3.1. Then we superimpose a small and tight dimple into which a part of the atoms thermalizes. If the atom number in the deep dimple trap is small compared to the reservoir, the overall temperature is unaffected by the small trap. Then the lowest energy levels in the system are occupied with a probability of almost unity. The required experimental tools for the dimple trap and the spilling technique to prepare the desired number of atoms will be presented in section 3.2.

3.1 Preparation of a degenerate Fermi gas

Dilute gases of alkali metals were the first candidates to be used for ultracold gas experiments. Apart from potassium, lithium is the only alkali metal having a stable and naturally abundant fermionic isotope. Its simple optical transition scheme and its tunable scattering properties allow us to cool the gas down to quantum degeneracy by first using radiation pressure and then evaporative cooling. These two steps will be explained in the following sections.

1. Titanium sublimator
2. Ion pump
3. Lithium oven
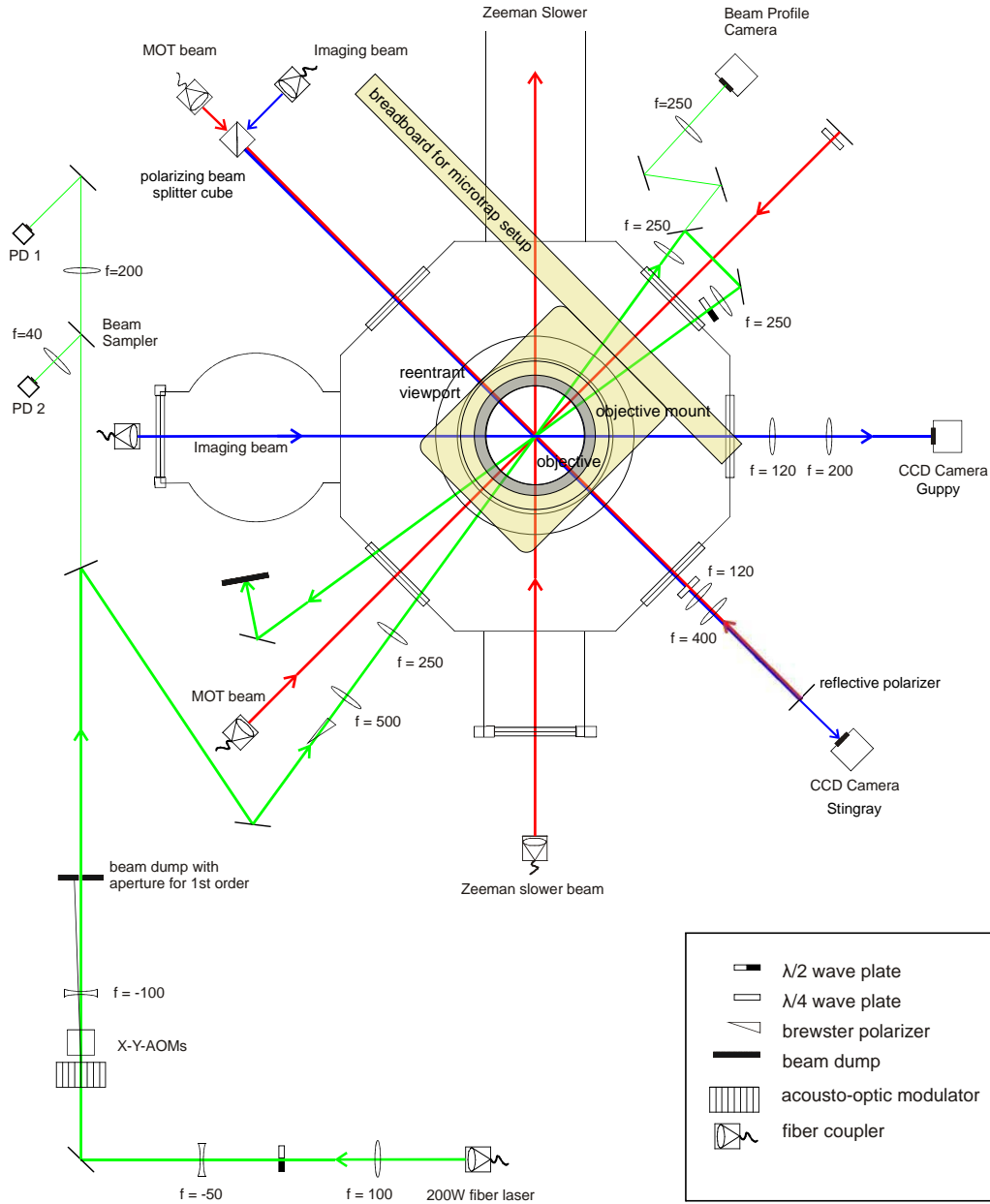4. Zeeman Slower
5. Octagon
6. Gate valve
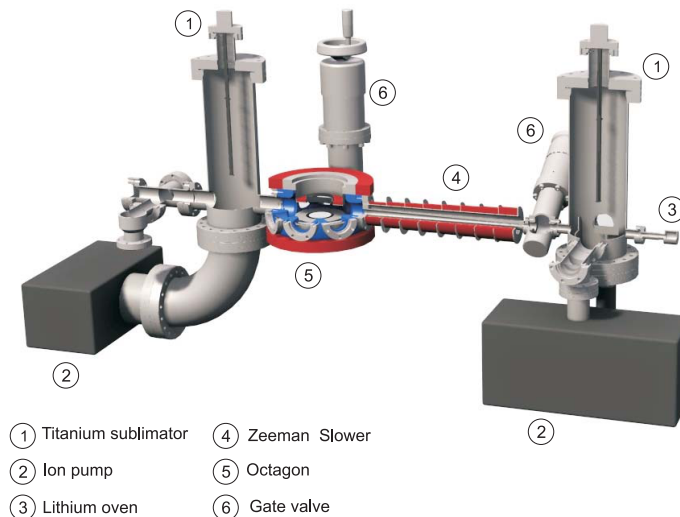
Figure 3.1: The vacuum chamber. The oven (No. 3) in combination with a drift tube forms an atomic beam going through the Zeeman slower (No. 4) to the main chamber (No. 5) where the atoms are captured and cooled to quantum degeneracy. The magnetic field coils for the Zeeman slower, MOT and Feshbach fields are marked in red. The first gate valves (No. 6) can be used to seal off the oven chamber. Furthermore, an oven shutter has been implemented between the oven and the gate valve for interrupting the atomic beam. Taken from [Ser07]

3.1.1 Laser cooling and trapping the atoms

By heating up solid lithium in a small oven to a temperature of $350\,°\text{C}$, we produce an atomic gas with a high vapor pressure. The lithium atoms enter the experimental chamber as an atomic beam which has been formed by a drift tube. A low vacuum pressure in this chamber is crucial to obtain sufficiently long lifetimes of the atomic samples for measurements to be performed. The low pressure is provided by two ion pumps with titanium sublimators as depicted in figure 3.1. In addition, the experimental chamber is coated with a non-evaporable getter coating (NEG). The drift tube between the oven and the chamber furthermore serves as a differential pumping stage and a movable oven shutter can block the atomic beam during the experimental sequence.

The atoms in the beam are first decelerated by radiation pressure: They absorb photons from a resonant laser beam that oppose their direction of motion and reemit them in random direction. The resulting net momentum slows the atoms down. To effectively decelerate the atoms down to an average velocity of a few m/s the laser beam has to be resonant to the optical transition over the entire distance. However, the optical transition is slightly shifted depending on the velocity of the atoms. To compensate for this we use the Zeeman slower coils, as depicted in figure 3.1, that provide a spatially varying magnetic field along the trajectory of the atoms.

Figure 3.2: Top view of the experimental chamber including the different laser beam paths. The near-resonant MOT and Zeeman slower beams are colored in red, beams for absorption imaging are in blue. The AVT Guppy F038B NIR CCD camera (Guppy) allows for fluorescence and absorption imaging perpendicular to the Zeeman slower axis. The AVT Stingray F033B CCD camera (Stingray) is only used for absorption imaging due to the stray light from the MOT beam. The far-red detuned dipole trap beam is marked in green. The X-Y-AOMs are used for power regulation. Above the chamber the breadboard with the mounted objective is illustrated (yellow). The third MOT beam has to traverse the objective before it is retro-reflected into the chamber.
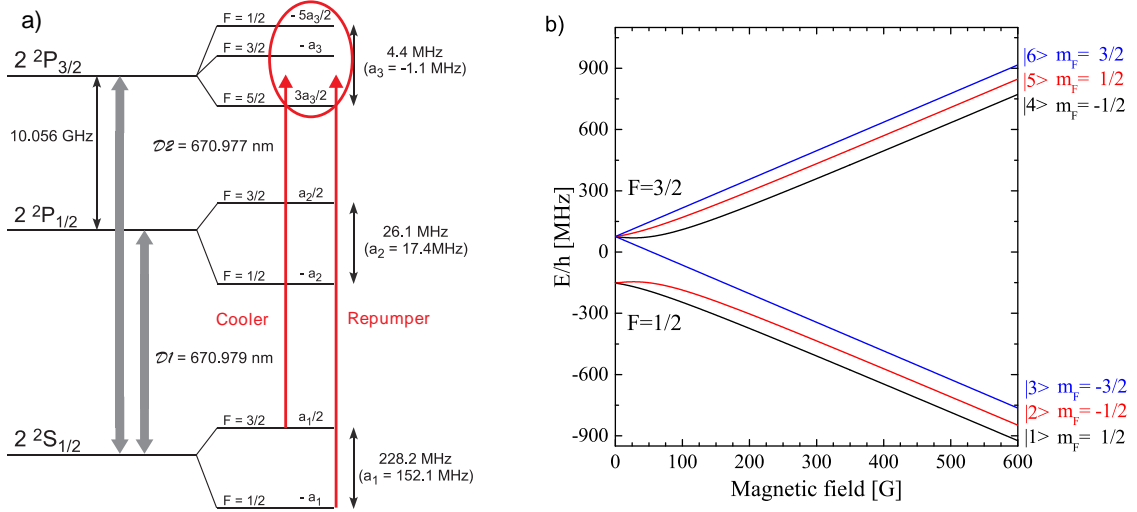
Figure 3.3: Electronic level scheme of ^{6}Li. (a) Laser cooling is performed on the D2-line. The cooler (repumper) light excites atoms from the $F = 3/2$ ($F = 1/2$) levels up to the P$_{3/2}$-level. Taken from [Geh03] and modified. (b) In non-zero magnetic field the hyperfine sublevels tune according to m_F in the low-field limit. In high-field they regroup with m_S as the coupling to the external magnetic field exceeds the internal coupling between the nuclear and the electronic spin. The states are denoted as $|1\rangle$ to $|6\rangle$ with rising energy.

The decelerated atoms enter the main chamber that provides high optical access. It is formed by a spherical octagon (MCF600-S0200800-A, Kimball Physics) with six CF40 viewports and two reentrant CF150 viewports on the top and the bottom. The small viewports provide an optical access of NA ≈ 0.15 whereas the reentrant viewports have a NA > 0.6 offering the possibility to implement a high-resolution objective.

After the deceleration in the Zeeman slower the atoms are captured and cooled in the magneto-optical trap (MOT). It consists of a magnetic quadrupole field created by a coil pair in anti-Helmholtz configuration and three slightly red-detuned retro-reflected laser beams. They cool the atoms and push them towards the center of the quadrupole field due to a spatially dependent light force. With this technique the reachable temperature of the atom sample is limited by the width of the driven optical transition. A detailed explanation to the basic principles of laser cooling is given in [Met99, Met03]. A top view of the setup including the laser beams of the magneto-optical trap is depicted in figure 3.2 and detailed descriptions of our experimental realization of the Zeeman slower and the MOT can be found in [Ser07].

Laser cooling of ^{6}Li is usually performed on the optical dipole transitions from $2^2\text{S}_{1/2}$ to $2^2\text{P}_{3/2}$ at $671\,\text{nm}$ named the D2-line. The single valence electron makes the electronic structure relatively simple and only few different laser frequencies are required as illustrated in the level scheme in figure 3.3 a. In low magnetic fields the electronic spin ($S = 1/2$), the angular momentum (L) and the nuclear spin ($I = 1$)

couple to the hyperfine spin F. This results in a set of non-degenerate hyperfine states.[1] For laser cooling we choose the transition from $S_{1/2}$, $F = \frac{3}{2}$ to $P_{3/2}$, $F' = \frac{5}{2}$, but as the splitting of the hyperfine states in the $P_{3/2}$-state is smaller than the natural linewidth Γ, the relaxation down to the $S_{1/2}$, $F = 1/2$ is significant. To avoid loosing atoms through this decay a second optical frequency serving as a repumper on the transition from $F = \frac{1}{2}$ to $F' = \frac{3}{2}$ with almost the same power as the cooling beam is used to close the cooling cycle. To cool and trap the atoms with the Zeeman slower and MOT, all laser beams contain these two frequencies. The optimal loading rate and atom number of the MOT are achieved for a red-detuning of cooler and repumper light of about 6Γ at a magnetic field gradient of $20\,\text{G/cm}$ provided by the MOT coils. To end up in a spin mixture of only $|1\rangle$ and $|2\rangle$ we switch off the repumper light slightly earlier and pump all the atoms into $F = 1/2$. After a loading time of $1\,\text{s}$ we detect about 2×10^8 trapped atoms in the MOT at a temperature of $200\,\mu\text{K}$.

For the characterization of the trapped atomic cloud we can make use of two differents methods to image the sample. We can collect the fluorescence light of the atoms that are captured in the magneto-optical trap. With this technique we can determine the number of atoms in the MOT. However the position and the temperature of the sample is given by the MOT itself. To obtain information about the temperature and position of colder atomic samples in the dipole trap (cf. section 3.1.2) we have to use absorption imaging. For this we shine a low-intensity beam of resonant light onto the atomic cloud. The absorption of the atoms results in a shadow picture that is imaged on a CCD camera (for details see [Ott10, Lom11]). From the obtained density profiles we can infer the position, the atom number and the temperature of the sample. For large samples this technique is suitable, but counting small atom numbers gets difficult due to the decreasing the signal-to-noise ratio. Thus, for counting small atom numbers in our system, we will use fluorescence imaging as described in section 3.2.3. In figure 3.2 the different imaging paths available in our experimental setup are shown. They allow for an exact determination of the cloud position in the chamber.

3.1.2 The dipole trap

Although the temperature of the sample in the magneto-optical trap is already reduced by six orders of magnitude, the phase space density is far away from reaching unity where quantum degeneracy is reached. For further cooling we transfer the atoms into a conservative potential. There, evaporative cooling can be performed which means releasing the hottest particles in the sample, e.g., by lowering the potential and subsequently rethermalizing the remaining atoms. Thus the average temperature of the sample is reduced.

---

[1]Note that the degeneracy of the sublevels m_F is lifted in non-zero magnetic field by the Zeeman effect. For the lowest two hyperfine states the coupling between I and S is weaker than the coupling to the external field above $B = 50\,\text{G}$ and the sublevels group with m_S, see figure 3.3 b. In the following the states are named $|1\rangle$ to $|6\rangle$ with rising energy shift.

There are two ways to create a conservative potential. One is via a magnetic field that traps atoms at its minimum[2]. Consequently only low-field seeking atoms can be confined in such traps and unfortunately these states have high loss rates due to dipolar relaxation processes. In addition, the experimental investigation in a purely magnetic trap is difficult as the interaction between the atoms usually adjusted via the magnetic offset field strength can not be varied at will. One can circumvent this by transferring the atoms into an optical trapping potential created by a focused laser beam.

To generate an optical force acting on atoms, it is not necessary to drive a resonant transition. Imposing an oscillatory electric field $\mathbf{E}(\mathbf{r}, t)$ on the atoms induces a dipole moment $\mathbf{p}$. The interaction between this field and the dipole moment is described by the potential $V_{\text{dipole}} = -\frac{1}{2}\langle \mathbf{E}\mathbf{p} \rangle$. If the electric field frequency is below the resonance, $\mathbf{E}$ and $\mathbf{p}$ are oscillating in phase and the potential becomes attractive. For frequencies above the resonance the potential becomes repulsive. The exact dipole potential is

$$V_{\text{dipole}}(\mathbf{r}) = -\frac{3\pi c^2}{2\omega_0^3} \left(\frac{\Gamma}{\omega_0 - \omega} + \frac{\Gamma}{\omega_0 + \omega} \right) I(\mathbf{r}) \tag{3.1}$$

where $\omega_0/2\pi$ is the resonant transition frequency and $\omega/2\pi$ denotes the frequency of the trapping light. Γ is the transition linewidth, c the speed of light and $I(\mathbf{r})$ is the intensity distribution that determines the shape of the potential. In the limit of small detuning, the optical potential depth grows with decreasing $\omega_0 - \omega$, but we also observe photon scattering due to the trapping light which causes atom loss. Since the photon scattering rate Γ_{sc} is proportional to $(\omega_0 - \omega)^{-2}$ it is favorable to detune the trapping light far to the red (or blue) to reduce photon scattering. A detailed description of optical traps can be found in [Gri00].

For the sake of simplicity we decided to transfer the atoms directly from the MOT to the optical dipole trap. The temperature in the MOT is limited to at least $200\,\mu K$. The transfer is only efficient if the conservative trapping potential is significantly deeper than the kinetic energy of the atoms due to the temperature. Also, the spatial overlap with the MOT has to be sufficiently large. Therefore we compress the initially large and warm MOT by ramping up the magnetic field gradient, reducing the detuning to 3Γ and decreasing the power in the MOT beams. Nevertheless a beam power of about $200\,W$ at far red-detuned $1070\,nm$ is required to create a trap that is deep enough. The trap light is delivered by a Ytterbium doped-fiber laser (YLR-200-LP) from IPG Photonics. The optical trap is formed by a crossed-beam configuration with an intersection angle of $14°$ and a beam waist of $40\,\mu m$ resulting in an aspect ratio of about 1:10 (see figure 3.2).

For the later evaporation we control the beam power with two acousto-optic modulators (AOM). The deflected power going into the main chamber is then varied in power via the amplitude of the radio frequency for the AOMs. For feed-back small fractions of the dipole trap beam are detected on two photodiodes with different

---

[2] Remember Maxwell's law: the creation of a static magnetic field with a maximum is not possible.
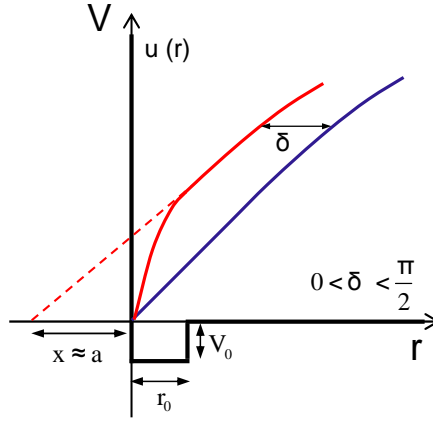
Figure 3.4: Scattering off a box potential. For zero potential depth the radial part of the wavefunction $u(r)$ is depicted in blue. For non-zero depth the wavefunction acquires a phase shift of δ. The associated scattering length a is the intercept between the dashed line and the abcissa. If a bound state in the potential gets close to the edge of the potential, the scattering length diverges. Taken from [Lom11] and adapted.

gain. With the two photodiodes we can stabilize the trap power over a large range down to very small trap powers.

All in all we transfer about 1% of the atoms into the dipole trap in a spin mixture of $|1\rangle$ and $|2\rangle$. By subsequently lowering the trap depth we evaporatively cool our sample.

3.1.3 Scattering properties of ^{6}Li

Effective thermalization of the sample is a indispensable prerequisite to make the evaporative cooling technique work. It requires well suited scattering properties of the atoms. In dilute gases inter-particle interaction is governed by two-body scattering as the average free path length exceeds by far the finite potential range.

An elastic two-body collision can be described by going to the center-of-mass frame of the two particles. Then, the stationary Schrödinger equation for a particle scattering off a spherically symmetric interaction potential can be solved. Due to the low temperatures of our samples the particles' de Broglie wavelength is on the order of $1\,\mu m$ while the interaction potential is much smaller. Thus the incoming plane wave does not probe the details of the interaction potential but only acquires a relative phase shift as depicted in figure 3.4. In addition, the low collision energy of the scattering partners enables only s-wave scattering as the centrifugal barrier for higher angular momenta cannot be overcome. The universal nature of such a two-body scattering process results in a single parameter that describes the entire collision, the s-wave scattering length a.

The exact value of a is determined by the phase shift which the incoming wave gets due to the interaction potential $V(r)$. This phase shift δ is mainly influenced by the
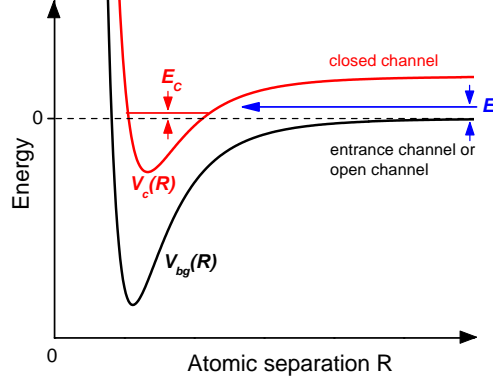
Figure 3.5: A two-channel scheme of a Feshbach resonance. The open channel is energetically accessible for the scattering process but the resulting background scattering length cannot be tuned. By tuning the energy of the closed channel a bound state energy E_c can be tuned to resonance with the continuum. Due to virtual coupling to this bound state the scattering length can be tuned and diverges for $E_c \to 0$. Taken from [Chi10].

energy difference between the highest bound states in the potential and the relative kinetic energy. δ is small if the highest bound state in the potential is energetically far away from the scattering energy, but as soon as this energy difference gets small, δ approaches $\pi/2$ and the scattering length diverges. In principle a can take any negative or positive values depending on the energy difference and therefore on the depth of the interaction potential.

Although the interaction between the scattering particles is due to an attractive potential, the phase shift can take values that make the effective interaction repulsive or attractive. In the scattering process the phase shift results in a change in relative momentum of the particles to positive or negative values. The resulting interaction energy of two scattering particles depending on the scattering length a amounts to

$$V_{\text{int}} = \frac{4\pi\hbar^2 a}{m} \,. \tag{3.2}$$

For negative scattering lengths this interaction is attractive whereas it is repulsive for positive scattering length. Thus the ability to change a not only results in a possibility to tune the interaction but also to choose between attraction and repulsion.

As the energy levels of bound states in the collision potential cannot be tuned with respect to its continuum the background scattering length a_{bg} is fixed. For nevertheless tuning the scattering length, we make use of the fact that there is more than one possible scattering potential. Scattering processes that are energetically accessible are called open channels, illustrated in figure 3.5. Entering the open channel, it is possible to couple virtually to an energetically forbidden (closed) channel. This coupling gets strong if the energy difference between the continuum and a bound state in the closed channel is vanishing. The relative energies between
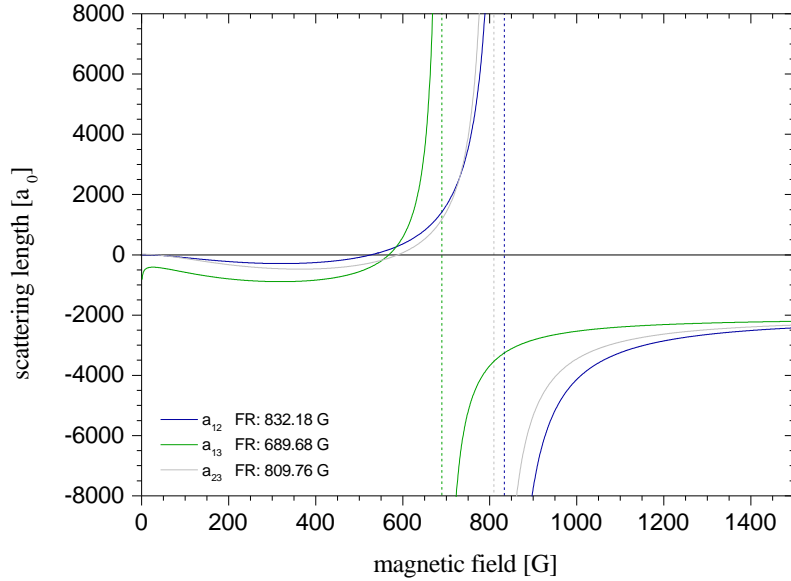
Figure 3.6: Feshbach resonances of ^{6}Li spin mixtures in the lowest three hyperfine states $|1\rangle$, $|2\rangle$ and $|3\rangle$. The broad Feshbach resonance is located at 832 G [Zü13]. At a magnetic field of $B \approx 523$ G the $|1\rangle$-$|2\rangle$ mixture is non-interacting. Taken from [Zü12a].

the collision channels depend on the internal quantum numbers of the scattering partners, e. g. the spin alignment. By applying a magnetic field B the difference in magnetic moment $\Delta\mu$ between the two channels results in a change in relative energy difference $\Delta\mu B = \Delta E$. It allows the variation of the scattering length as a function of the magnetic offset field [Chi10]

$$a(B) = a_{\text{bg}} - a_{\text{bg}}\frac{\Delta B}{B - B_0} \tag{3.3}$$

where B_0 is the magnetic field offset of the resonance position. ΔB is the width of the resonance and depends on the coupling and the difference in magnetic moment.

The scattering process of two particles depends also on the quantum statistics of the collision partners. In the collision process of two identical fermions the total wavefunction has to be anti-symmetric. For vanishing angular momentum the two possible final configurations of the two-body collision interfere destructively and the resulting scattering cross-section is zero. Thus identical fermions cannot collide via s-wave scattering. A detailed calculation can be found in [Dal99]. To obtain a finite scattering cross-section for s-wave scattering of fermions, they have to be distinguishable.

In the following we will only consider the scattering between the hyperfine states $|1\rangle$ and $|2\rangle$ of ^{6}Li which can collide in a singlet or a triplet configuration. For low magnetic offset field, both channels are energetically allowed and collisions occur in a superposition of both configurations. The background scattering lengths of

$|1\rangle$ - $|2\rangle$ mixture is $a_{\mathrm{bg,s}} = 39a_0$ for the singlet and $a_{\mathrm{bg,t}} = -2240a_0$ for the triplet configuration, where a_0 is the Bohr radius. In the high magnetic field range, the spins get aligned by the external magnetic field and only the triplet configuration is energetically accessible. The channels can be coupled and the scattering length can be tuned by the magnetic offset field. At $832\,\mathrm{G}$ [Sal13] this mixture shows a broad Feshbach resonance where the scattering length diverges, see figure 3.6. But also at higher fields of up to $B = 1400\,\mathrm{G}$ the absolute value of the scattering length remains large due to the large background scattering length of the triplet state. Below the resonance a has a minimum at $B = 300\,\mathrm{G}$ and at a field of around $B = 523\,\mathrm{G}$ the sample is non-interacting. The mixtures of $|2\rangle$ - $|3\rangle$ and $|1\rangle$ - $|3\rangle$ show similar curves of the scattering length over the magnetic field.

3.1.4 The magnetic offset field

The magnetic offset field for the adjustment of the scattering length is provided by two coils approximately in Helmholtz configuration. They consist of fifteen windings of a 5mm × 1mm copper wire and are glued onto water-cooled heat sinks with diamond-filled epoxy. Since they are mounted in the outer rims of the reentrant viewports, they do not decrease the optical access and are nevertheless as close as possible to the atomic sample. The current for the coils is provided by a SM15-400 (Delta Elektronika) power supply and stabilized by a current transducer and a digital feedback loop [Koh08].

The Helmholtz configuration provides a magnetic field with a maximum in the radial plane. Thus, it acts as a confining field on the high-field seeking hyperfine states. Since the distance of the coils is slightly larger than required for Helmholtz configuration, the field is anti-confining around the center position in axial direction with almost the same absolute value of curvature. For a detailed description of the magnetic field, see [Ser07, Zü09, Lom11].

With currents up to $I = 400\,\mathrm{A}$ the coil pair can produce magnetic offset fields from $0\,\mathrm{G}$ to $1400\,\mathrm{G}$ with a sufficiently high stability. By switching the current direction in one of the coils we can also produce a gradient field. We use this to increase the magnetic field gradient in the MOT compression phase, see section 3.1.2.

For the installation of the new and large high-resolution objective the Feshbach coils had to be replaced. In the course of this a new feedback loop scheme was implemented which was later used for the measurements with the new objective. Further details concerning the stabilization are described in section 4.4.1.

3.1.5 The evaporation scheme

With the scattering length a being freely tunable via the magnetic field we can maximize the thermalization rate required for efficient evaporative cooling. Thermalization is fast for a large scattering rate and thus for a high scattering cross-section. The scattering cross-section grows with a^2 and thus we can tune the system to strong repulsive or attractive interaction for efficient evaporative cooling.

The scattering length diverges on the Feshbach resonance. For evaporation we go to a field of 760 G. As soon as the temperature of the sample gets down to the order of the binding energy of dimers the formation of molecules starts. At this field we can achieve a pure molecular BEC in about 3 s, loosing about a factor of 10 in atom number. The preparation of a molecular BEC is useful for diagnostics of our setup but for the preparation of our few-body system it is of no use.

Instead we need a weakly interacting degenerate Fermi gas. In principle one could dissociate the cold molecules by ramping to higher magnetic field, but above the Feshbach resonance the interaction is still strong. Only at fields lower than the Feshbach resonance field the scattering length gets small. However, by a magnetic field ramp to lower fields the sample ends up in the molecular branch.

To prepare a weakly interacting Fermi gas we have to avoid the molecule formation. We start evaporative cooling at the resonance until the first molecules start to form after 1.8 s. Then we jump to $B = 300$ G where the scattering length is negative. Due to the large absolute value of a thermalization still works but is less efficient. It takes another 4.5 s until we get about $T/T_F = 0.5$ with 2×10^4 atoms per spin state.

In a Fermi gas further evaporation gets more and more inefficient since the lower temperature the Fermi sphere has already filled up and the number of unoccupied states is small. Scattering into the unoccupied states at the edge of the Fermi sphere gets less probable. To reach higher degeneracy in the sample we superimpose a tight optical dimple trap [SK98]. In the following we exploit this technique and use the dimple trap to prepare a few-fermion system with high fidelity.

3.2 The microtrap

The superposition of the large dipole trap with a small dimple trap is the crucial step to increase the degeneracy of our sample. The dimple trap is a far red-detuned optical trap which creates a dipole potential as presented in section 3.1.2. It is formed by one single tightly focused Gaussian beam. The intensity distribution determines the potential form

$$V(\mathbf{r}) \propto \frac{I_0}{\pi w^2(z)} \exp\left(-2\frac{\rho^2}{w^2(z)}\right) \tag{3.4}$$

where ρ is the radial and z the axial coordinate. $w(z)^2 = w_0^2(1 + (\frac{z}{z_\mathrm{R}})^2)$ describes the waist of the Gaussian beam in axial direction with w_0 the focus waist and z_R the Rayleigh length. I_0 is the peak intensity of the beam.

With a focus waist in the range of few micrometers and moderate laser powers the trap frequencies characterizing the potential are much higher than in the dipole trap. This means that the level spacing in the trap is large. So, only a low number of atoms fit into the microtrap. Therefore the superposition with the reservoir and the subsequent thermalization does not influence temperature T of the sample. As the depth of the dimple trap exceeds the final depth of the large dipole trap the Fermi energy is completely governed by the dimple trap $T_\mathrm{F} \approx T_\mathrm{F, \, dimple}$. After the atoms

have thermalized into the dimple trap, the quantum degeneracy of the combined trap system has increased as $T/T_{\text{F, dimple}} < T/T_{\text{F, dipole}}$.

The high quantum degeneracy is equivalent to an occupation probability of almost unity for the lowest trap levels. We exploit this fact for the deterministic preparation of few fermions in the lowest levels of the dimple trap [Ser11b]. We tilt the trapping potential and spill all the atoms from higher lying energy levels ending up with a distinct number of atoms that remain trapped. The fidelity of this atom number preparation depends on the level spacing and on the stability of both the tilt and the trap depth. The smaller the trap focus is the better we can prepare our sample and the less stability is required. So our goal is to set up a dimple trap, in the following called *microtrap* with a small waist and a stabilized depth. The first generation of the microtrap and the spilling technique is described in section 3.2.2. For increasing our preparation fidelity we developed a high-resolution objective to create an even smaller focus. Its preparation performance has been investigated in the course of this thesis and is presented in section 5.1.

3.2.1 The first generation microtrap setup

The first generation microtrap is created by a two-lens objective with a numerical aperture of NA= 0.36. It focuses a collimated 1064 nm beam through the vacuum window of the upper reentrant viewport into the main chamber, see figure 3.7. In a distance of 40.7 mm behind the objective the focus is superimposed with the dipole trap. For an intensity of 240 µW the measured trap frequencies of the microtrap are $\omega_r, \omega_a = 2\pi \times (13.2 \pm 1.1, 1.4 \pm 0.1)$ kHz. This results in a waist of $w_0 = 1.8$ µm and an astigmatism of a 10% between the two tight trap axes. The aspect ratio amounts to about 10.

For deterministic preparation the depth of the microtrap must be very stable. Intensity noise on the laser light in the range of the trap frequencies would heat the atoms into higher levels. The infrared trapping light is provided by a Mephisto-S 500 NE (INNOLIGHT) which has a low intensity noise level (measured RIN<-120 dB/Hz for f<300 kHz [Nei13]). Furthermore, the laser power for the microtrap is stabilized by reflecting half of the beam power in front of the microtrap objective onto a photodiode. With this signal we stabilize the microtrap by regulating the input power with an acousto-optic modulator. The exact scheme is shown in figure 3.8.

For loading the microtrap we start with a mixture of atoms in states $|1\rangle$ and $|2\rangle$ in the dipole trap. After evaporation (cf. section 3.1.5) we end up with 2×10^4 atoms per spin state at a temperature of about 250 nK. This corresponds to $T/T_F = 0.5$. Within 100 ms we adiabatically ramp on the microtrap and let the sample thermalize for 20 ms at a magnetic offset field of $B = 300$ G . For detailed description of the adiabatic ramp see [Ser11a, Zü12a]. With a trap light power of $P = 240$ µW the quantum degeneracy in the microtrap amounts to $T/T_F = 0.08$. Subsequently the reservoir is removed and about 600 atoms remain in the microtrap. We ramp the magnetic offset field to $B = 523$ G where the particles are non-interacting.
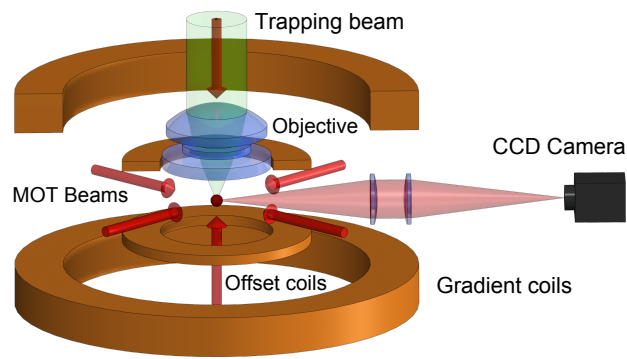
Figure 3.7: A detailed view of the experimental configuration for the microtrap creation and atom detection. The trapping beam is shone through the top vacuum window of the reentrant viewport onto the atom sample. The gradient coils are used for the spilling, the offset coils set the interaction strength between the atoms. The atom number detection is done by loading the atoms back into a MOT and capturing their fluorescence light with a CCD camera. Taken from [Ser11a].
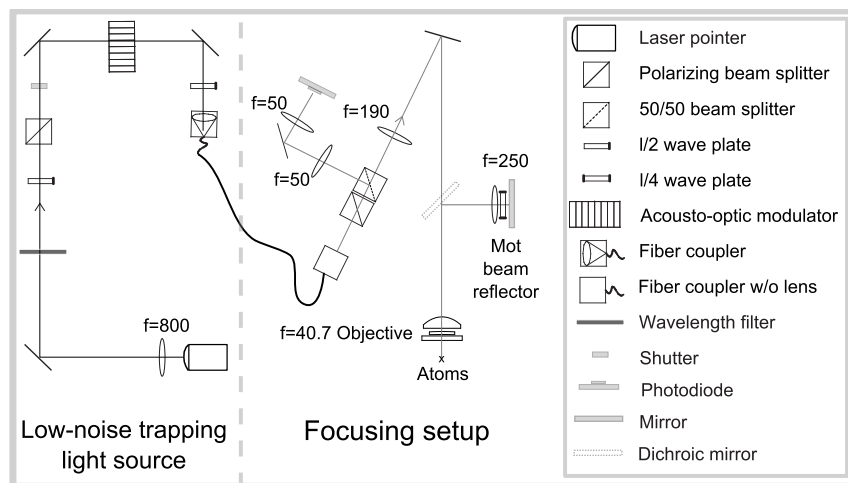
Figure 3.8: The microtrap setup. The power stabilization and creation scheme of the trapping beam are illustrated. The power is stabilized by passing the beam through an AOM. On the focusing setup the polarization of the incoming beam is cleaned and half of the power is reflected by a 50/50 beamsplitter for the power detection on a photodiode. The beam is collimated with a lens of $f = 190\,\text{mm}$ and then focused through the objective onto the atoms. Taken from [Ser11a].
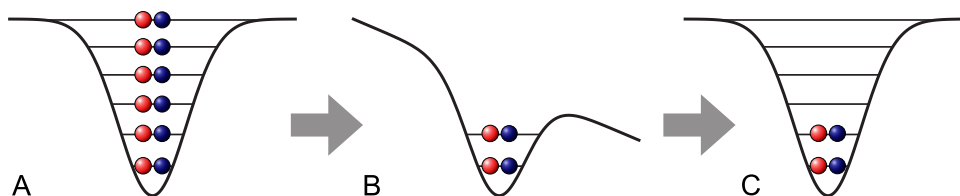
Figure 3.9: The spilling technique. A two-spin state quantum-degenerate gas
of fermions is loaded into the microtrap (A). By applying a magnetic field
gradient and fine-tuning of the potential depth (B) one can selectively prepare
a few-fermion system in its ground state (C). Taken from [Ser11a].

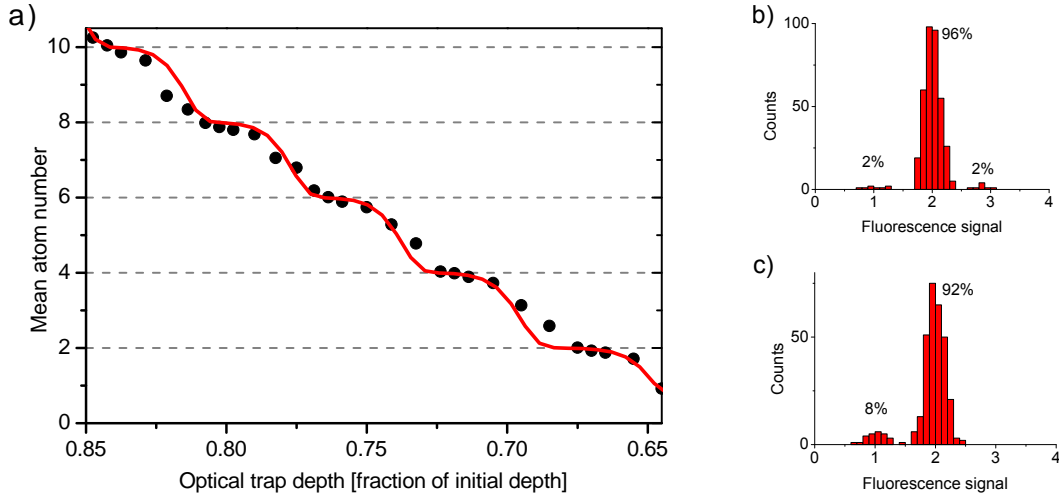## 3.2.2 Deterministic preparation of few fermions

The remaining 300 atoms per spin state fill up the microtrap according to the Pauli
principle. To spill the trap down to a certain energy level, we deform the trapping
potential such that the higher levels become unbound, as depicted in figure 3.9. We
do this by applying a magnetic field gradient of $B' = 18.92\,\mathrm{G/cm}$ with the MOT
coils[3] along the weakly confining axial direction of the microtrap. This gradient
couples to the atoms via their magnetic moment. At high magnetic offset field the
magnetic moments of the two spin states are approximately equal and the potential
deformation is almost the same from both hyperfine states[4].

With the applied magnetic field gradient about 20 atoms remain in the trap. For
precise selection of a distinct number of atoms we additionally decrease the potential
depth. For this we lower the laser power within 8 ms to a height where all the energy
levels down to the desired one become unbound and the atoms escape or tunnel out of
the potential. The tunneling times of the atoms in the bound levels below are much
larger so that they stay in the trap. After a hold time of 25 ms the potential depth
is ramped up to the initial value in another 8 ms. For atom number detection we
transfer the atoms into a small magneto-optical trap (MicroMOT) which is described
in section 3.2.3.

By applying a magnetic field gradient and fine tuning the potential depth we
are able to prepare up to 10 atoms in the ground state with a fidelity about 90%
[Ser11b]. Figure 3.10 a shows the number of atoms we prepare over the potential
depth normalized to the initial depth. With our stabilization setup we can tune
the optical power in the trap precisely enough to distinguish the doubly occupied
trap levels. By appropriate choice of the potential depth, we can prepare a distinct
even atom number. The two-atom steps also indicate that excitations in the radial
direction of the trap are frozen out and we have a quasi one-dimensional trap of axial
excitation levels. In the limit of one dimension the steps have also been simulated
indicated by the red solid line in figure 3.10 a. Detailed descriptions of the simulation

---

[3] The applied gradient is rather small. After the inset of the new Feshbach coils and the change of
the stabilization scheme, described in section 4.4.1 we are able to apply higher gradients.

[4] For the exact characteristics, see figure 3.3. At $B \approx 23\,\mathrm{G}$ the magnetic moment of $|2\rangle$ is zero and
the magnetic field gradient only couples to $|1\rangle$. There, we can prepare imbalanced samples.

Figure 3.10: Deterministic control over occupied quantum states. Figure (a) shows the detected atom number as a function of the optical trap depth in the spilling process. Clear two-atom steps are visible indicating a deterministic preparation of filling number. (b) Preparation fidelity of two atoms in the lowest energy state. For estimating the possible excitation due to heating by the spilling process itself, the fidelity after a second spill is shown in figure (c). Taken from [Ser11a].

can be found in [Ser11a].

Two atoms can be prepared in the lowest trap level with 96% fidelity (cf. figure 3.10 b). In 2% of the cases 1 or 3 atoms remain in the trap, respectively. To make sure that we did not heat up the system during preparation we spill the trap a second time. This still yields a fidelity of 92% for the 2-atom system, as shown in figure 3.10 c. From this we conclude that we prepare the system in the ground state with high fidelity and heating is small.

3.2.3 Atom number detection

To detect numbers of atoms on the order of one we transfer the sample back into the magneto-optical trap and use fluorescence imaging. For reliable atom counting the recapture into the MOT has to be efficient and the measurement of the fluorescence photons has to be optimized concerning the signal-to-noise ratio.

To raise the signal of the fluorescence imaging of a MOT, the number of detectable photons can be increased by a large exposure time on the camera and a reduced red-detuning to the optical transition. The noise can be suppressed by minimizing the area on the camera, where fluorescence light is detected by compressing the MOT via a stronger magnetic field gradient ($B' = 250\,\mathrm{G/cm}$ in our case). Furthermore, a reduction of the stray light during the detection can be achieved by decreasing the size and power of the MOT beams.

Limited by the imaging optics, we can collect only 0.8% of the emitted fluorescence
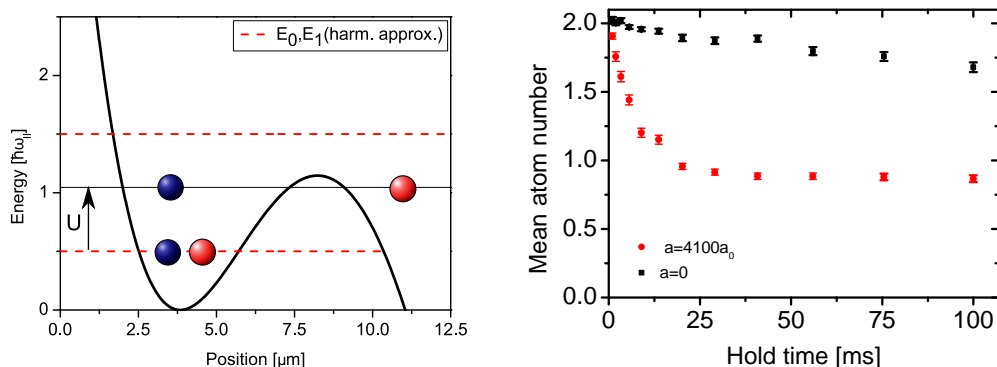
Figure 3.11: Influence of the interaction energy on the level position. Figure (a) illustrates the energy level shift due to inter-particle interaction U of a two-particle system in the ground state. The effective tunneling barrier can be deduced by the measurement of the tunneling time. Figure (b) shows such a measurement of the tunneling time over the mean atom number. Precise knowledge of the potential shape and a WKB calculation enable the measurement of the interaction strength U. Taken from [Ser11a].

photons on a CCD camera (AVT Guppy F038B NIR), see figure 3.7. After an exposure time of $0.5\,\text{s}$ we integrate the fluorescence signal of the MOT. For counting the atom number the detected fluorescence signals are binned into a histogram. It shows clearly distinguishable peaks that we identify as discrete atom numbers separated by 6σ assuming gaussian distributions. The reliability of the atom number detection can in principle be limited by the lifetime of the atoms in the MOT. In our setup, however it exceeds $250\,\text{s}$ and is thus significantly larger than our detection time.

The recapture of the sample into the MOT is affected by the spatial overlap with the microtrap and the force that pulls the atoms into the MOT. For the transfer we ramp up the magnetic field gradient to $B' = 250\,\text{G/cm}$ as fast as possible. The capture efficiency is hard to determine quantitatively. However, we estimate a lower limit of $98(1)\%$ considering the high measured preparation fidelity of few atoms.

3.2.4 Energy- and spin-dependent detection methods

With the fluorescence imaging in the MicroMOT we are able to detect the number of atom number that we prepared in our microtrap. However, we cannot distinguish their spin states and the atom detection does not reveal any information about the energy levels the atoms have occupied. We have to conclude all these information by trap spilling and subsequent atom counting.

The determination of the energy of the trap levels in our system is the first tool we developed. The common energy level of two fermions with different spin is shifted by the interaction energy U between them, as depicted in figure 3.11 a. For precisely measuring this shift, we can use the fact that the atoms can also tunnel through

the potential well within a certain time if their energy is very close to the barrier height. The tunneling time is thus a direct measure of the energy difference to the barrier height. We prepare a sample with few atoms, turn on the interaction and set a certain barrier height. The tunneling rate is then measured by holding this tilted potential for a certain time, then ramping the barrier up again and counting the remaining atoms. We plot the mean atom number of the different hold times. As depicted in figure 3.11 b, the mean number of atoms remaining in the trap decreases faster for stronger repulsive interaction. The level was shifted upwards due to the interaction. By comparing the tunneling times of a non-interacting system with an interacting system, one can deduce the exact energy shift, if the potential shape is known [Ser11a]. With the tunneling measurement and subsequent WKB calculations, we could observe fermionization of two distinguishable fermions [Zü12b].

Another issue is the determination of the spin state in the system in spite of spin-insensitive atom number counting. Suppose we have one atom of either state $|1\rangle$ or $|2\rangle$ in the trap. If we can selectively spill one atom species, subsequent counting of the remaining atoms directly tells us, in which state the atom was. As the magnetic field gradient couples to the magnetic moment of the atoms the selective spilling of state $|1\rangle$ can be performed at the magnetic offset field of $B \approx 23\,\text{G}$. There, the magnetic moment of state $|2\rangle$ is zero and thus the potential is not deformed for atoms in this hyperfine state during the spilling process.

Recently we used this method to prepare an imbalanced few-particle Fermi gas with only one minority atom and several majority atoms. We then could determine the inter-particle interaction strength as a function of the scattering length and the majority particle number. Here, the interaction energy was measured by its shift of the rf transition frequency between the two hyperfine states [Wen13].

These tools of measuring the energy in the system and the spin-selective spilling demonstrate the detection possibilities in our system although we can only count atoms. Together with the deterministic preparation of the atom samples in the ground state we have thus a highly controllable system at hand to investigate few-body phenomena in quantum mechanics. The low entropy per particle in the system also provides a way to explore unconventional phases of condensed matter physics like the Néel phase.

Chapter 4

A new microtrap setup

The objective of the microtrap setup described in the previous chapter was supposed to be a temporary solution until the high-resolution objective designed in [Ser11a] had been assembled. In spite of the relatively large focus size of $2\,\mu m$ we were able to demonstrate high preparation fidelity with this objective [Ser11b] and to study the physics of few-fermion interactions in quasi-1D systems [Zü12a]. Replacing it with a high-resolution objective provides us with a much smaller focus with fewer abberations which gives us better control over the preparation procedure. However, our goal was not only to improve the quality of our optical trap, but also to increase its flexibility. An acousto-optic deflector (AOD) enables us to manipulate the shape of our focus and allows the creation of multiple independently controllable wells, as depicted in figure 4.1. With these capabilities we will be able to investigate, e. g., Fermi-Hubbard physics with tunable tunneling parameters on experimentally accessible time scales.
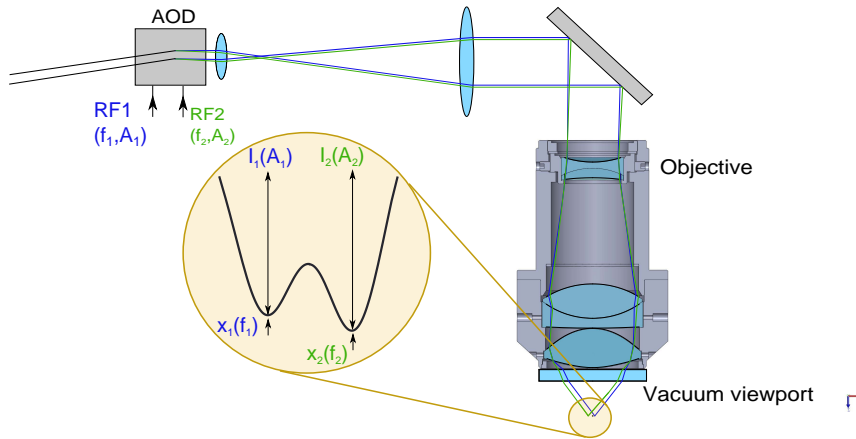
Figure 4.1: Working principle of the new setup. An acousto-optic deflector (AOD) provides several trap beams which are controlled via radio-frequency input. After beam expansion by a telescope they are focused by a high-resolution objective into the vacuum chamber. The objective translates the angular differences between the beams into a shift of the position of focus. This creates an array of microtraps whose separations and relative depths can be tuned by the frequency and amplitude of the rf signals applied to the AOD.

wavelength	$\lambda = 1064\,\mathrm{nm}$	$\lambda = 671\,\mathrm{nm}$
focal length	$20.3\,\mathrm{mm}$	$20.3\,\mathrm{mm}$
image distance	∞	∞
diameter field of view	$200\,\mathrm{\mu m}$	$200\,\mathrm{\mu m}$
max. diffraction limited NA	0.6	0.6
entrance aperture diameter at max. NA	$24.4\,\mathrm{mm}$	$24.4\,\mathrm{mm}$
resolution	$1.08\,\mathrm{\mu m}$	$0.68\,\mathrm{\mu m}$
waist of focus	$0.72\,\mathrm{\mu m}$	$0.45\,\mathrm{\mu m}$

Table 4.1: The nominal design parameters of the high-resolution objective. Taken from [Ser11a].

This chapter presents the characterization of the components and the alignment of the new microtrap setup. The properties of the high-resolution objective and the optical setup providing the trapping beam are presented in section 4.1 and 4.2 focusing on a quantitative determination of the wavefront error sources. Section 4.3 explains the working principle of the acousto-optic deflector and the creation of double-well potentials and more complex potentials. In section 4.4 the integration of the new microtrap setup into the existing experiment is summarized.

4.1 The high-resolution objective

We intend to create microscopic potential structures by using an objective for focusing the trapping beams. The required numerical aperture entails a sub-micron imaging resolution. A chromatic correction of the objective for the imaging light allows for high-resolution imaging.

The required objective with its largest possible NA provides diffraction-limited performance at 1064 nm and 671 nm including chromatic corrections. Additionally it needs an effective focal length larger than 20 mm as it will be placed outside the vacuum chamber. Hence, it also has to be corrected for the 6 mm vacuum window. An objective which fulfills all the requirements has been developed in [Ser11a] and consists of a large asphere for focusing and two achromats for expanding the incoming beam. The nominal parameters are listed in table 4.1 and the detailed design is depicted in figure 4.2. The high numerical aperture makes the objective's performance sensitive to its exact alignment. Since focus diagnostics are impossible once the objective has been added to the vacuum chamber a detailed and deterministic alignment procedure has been devised.

After the design procedure a detailed characterization of the manifactured objective was necessary in order to estimate the expected performance in the experiment and recognize potential limitations and sensitivities. The two objectives assembled by Jenoptik are subsequently denoted as 'BA1001' and 'BA1002' and have both been tested.
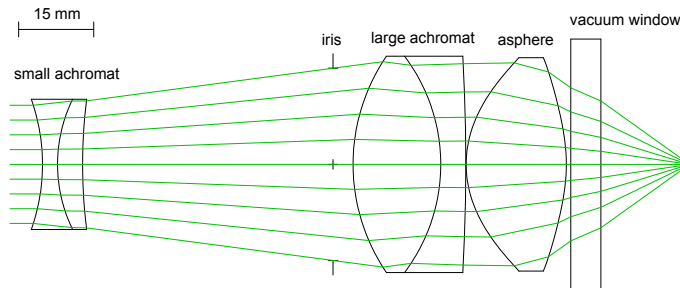
Figure 4.2: The high-resolution objective consists of a large asphere lens providing an *NA* = 0.6 at a focal length of 20.3 mm. The large and the small achromatic doublet decrease the required incident beam size to a diameter of 24.4 mm. The entire objective is corrected for the 6 mm thick vacuum window located 2 mm behind the asphere and for the chromatic shift between the two design wavelengths 1064 nm and 671 nm.

4.1.1 Determination of wavefront errors

The high-resolution objective has been designed to produce a diffraction-limited focus for the microtrap. Wavefront distortions in the objective can degrade the quality and the size of the focus. They are measured by the deviation from a spherical reference wavefront created by a perfectly focusing optical device. However, for very small wavefront distortions the form of the focus would not be recognizably worse. It can be shown that the deviation from the intensity distribution of a perfect focus only becomes visible for errors greater than 0.07λ [Mah82].

We measure the wavefront created by the objective by means of interference. Therefore, we set up a Michelson interferometer, see figure 4.3. One of the two paths contains the objective aligned together with a vacuum window and a concave spherical mirror which is positioned behind the focus. The beam hits the reflective sphere perpendicularly if its curvature corresponds to the wavefront curvature of the beam at that position. Thus, assuming that all the other optical elements and the sphere are perfect the resulting interference picture directly shows the double wavefront errors of the objective. This measurement has been presented in [Kli12] and shows that the errors are $< \lambda/4$.

However, it is difficult to quantitatively determine the absolute value of the wavefront error as the measurement does not show the full contrast which corresponds to $\lambda/4$ in optical path difference. For a second measurement we introduced a slight offset to the position of the sphere in order to get rings on our interference pattern as shown in figure 4.4. In case of a perfect objective the rings are concentric and circular. Any deviation from that can be attributed to higher orders of wavefront errors. In our measurement we observe no deviation from a circular wavefront larger than $\lambda/8$ up to a diameter of 20 mm for both objectives. The deviation from concentric fringes is clearly larger in the objective BA1002 with about $\lambda/4$. The results are in agreement with the mentioned measurements in [Kli12] and shows the high performance level of the objectives.
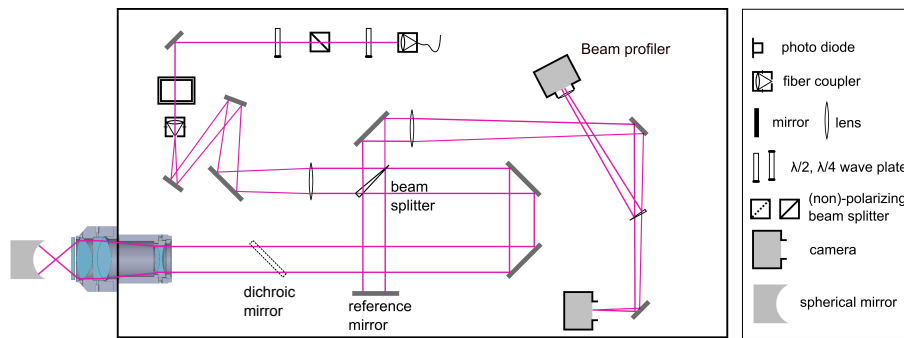
Figure 4.3: Optical setup for the wavefront analysis of the objective. The objective together with a spherical mirror implemented in one path of a Michelson interferometer. The interference pattern which indicates wavefront errors is imaged on a beam profiler camera.
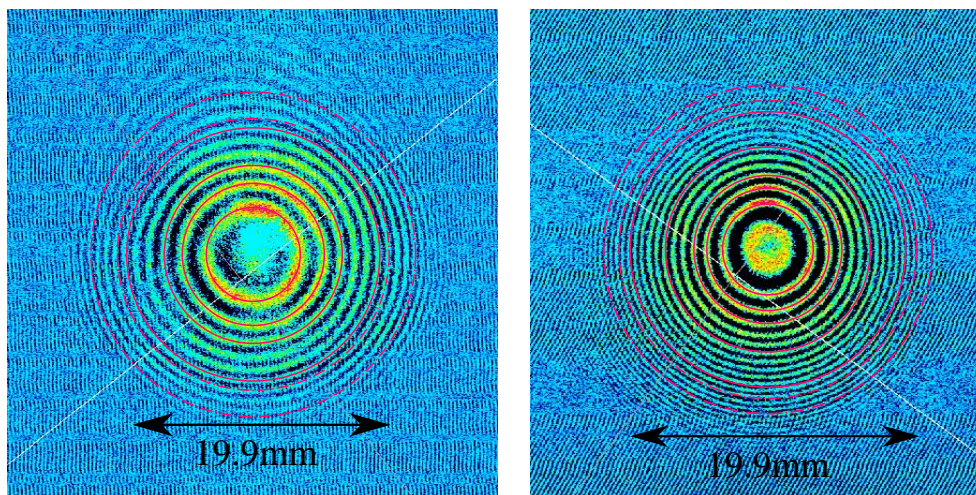
Figure 4.4: Measurement of the wavefront errors (left: BA1001, right: BA1002). The objective is installed in a Michelson interferometer with a spherical mirror behind the objective's focus. The position of the sphere is slightly displaced with respect to the position where the wavefront curvature corresponds to the sphere curvature which results in circular fringes with a spacing of $\lambda/2$. Deviations from the concentric circles (red) indicate wavefront errors. Both interferometer patterns show no deviation from the circular form by $> \lambda/8$ upto to a diameter of 20 mm (solid lines). The circular fringes of the objective BA1002 deviate by $\lambda/4$ from the concentric configuration.

4.1.2 Measurement of the resolution

The quality of an optical device also becomes evident by its resolution of a point-like object. In our case this is of interest for a later usage for fluorescence imaging.

The resolution r of an imaging system is defined as the minimum distance between two point sources that can still be distinguished. Diffraction fundamentally limits the resolution as the image of the intensity distribution of a point source has the form of an Airy disc. The size of the pattern depends on the size of the light cone that is captured by the imaging device. Thus, r is the distance between the maximum and its adjacent first minimum of the diffraction pattern, corresponding to

$$r = 1.22 \, \frac{\lambda}{2NA} \tag{4.1}$$

with the numerical prefactor coming from the two-dimensional geometry of the Airy disc, λ the wavelength of the light and the numerical aperture NA.

To determine the resolution of an objective a point source is imaged delivering the so-called point spread function (PSF). Therefore one has to choose an object that is much smaller than the nominal resolution. In [Kli12] an 800 nm large pinhole was used for this measurement but the influence of the finite size of the object on the measurement was not clear. For more reliable values we used a gold grating [Ott06] with 650 nm holes in a relative distance of 20 µm that we illuminate from the back with laser light of 1064 nm and 671 nm[1] and set into the focal plane of the objective. The image is detected on a CCD camera (Thorlabs beam profiler BC106-VIS, pixel size 6.45 µm) with a lense of $f = 750$ mm (Melles Griot, wave front error $< \lambda/10$).

In table 4.2 the measured resolution of both objectives are compared with the resolution of the objective BA1002 measured with the pinhole. Within the errors both measurements give approximately the same results. The objective BA1001 shows a slightly better resolution than the objective BA1002 where we observed abberation in the PSF (cf. figure 4.5). However, the deviations from the nominal values are significant for both objectives.

Note that a direct examination of the alignment with direct feedback from focus diagnostics will be impossible when the objective is installed in the experiment. This requires a passive alignment which has also been applied for all characterization measurements presented in this section. The vacuum window and the lens planes in the objective are designed to be parallel. First, the beam is adjusted to be perpendicular to the vacuum window which provides a plane of reference. Next, the objective is mounted before the vacuum window and a dichroic mirror is placed upon the casing of the objective. The plane of this mirror can be adjusted to be parallel to the reference plane by minimizing the interference fringes.

With the test setup one has the possibility to align the objectives angle 'actively'. This means that the tilt angle is aligned for obtaining a symmetric PSF on the camera. In the pinhole configuration we could not see an improvement of the resolution by

---

[1]The adjustment for the measurement gets much easier due to the grating and the magnification can be determined with high accuracy.
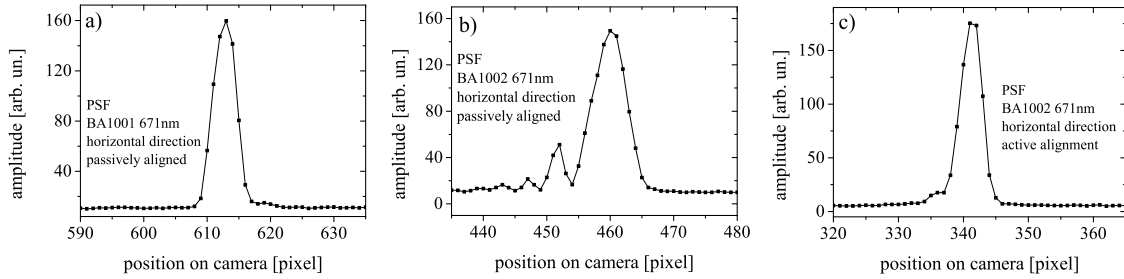
Figure 4.5: Intensity profiles of the PSF in horizontal direction at 671 nm measured with the gold grating. (a) shows the profile of the passively aligned objective BA1001. In (b) clear abberation can be detected in the PSF of the passively aligned objective BA1002. (c) shows the result for an active alignment of the objective BA1002. Qualitatively it does not differ from (a).

| λ | BA1002 pinhole [Kli12] | | BA1002 grating | | BA1001 grating | |
	671 nm	1064 nm	671 nm	1064 nm	671 nm	1064 nm
x-prof.	1.08 ± 0.07	1.48 ± 0.09	1.51 ± 0.10	1.61 ± 0.10	1.12 ± 0.10	1.42 ± 0.10
y-prof.	1.05 ± 0.04	1.59 ± 0.11	1.21 ± 0.10	1.51 ± 0.10	1.12 ± 0.10	1.33 ± 0.10
nom.	0.68	1.08				

Table 4.2: Measurement of the resolution in µm by imaging the point spread function of both objectives. The measurement was proceeded with an 800 nm large pinhole [Kli12] for 'BA1002' and a gold foil with a grating of 650 nm large holes for both objectives. For the measurement the objectives were aligned passively to the vacuum window. Within the errors the measurements give approximately the same results. The objective BA1001 performed slightly better.

| λ | BA1002 actively aligned | |
	671 nm	1064 nm
x-prof.	1.01 ± 0.10	1.21 ± 0.10
y-prof.	1.01 ± 0.10	1.21 ± 0.10
nom.	0.68	1.08

Table 4.3: Resolution measurement by imaging the point spread function of the objective 'BA1002' after active alignment in µm. The data was taken using the gold foil. The results are significantly better than for the passive alignment and closer to the nominal values.

the active alignment. With the gold foil the active alignment, however, improved the PSF drastically and the measured resolution for the objective BA1002 was much closer to the nominal parameters. Thus, we conclude that taking the tube of the objective as a reference plane for the parallel alignment does not deliver the best results. This is probably caused by a tilt of the symmetry axis of the lens system with respect to the tube axis. It will be challenging but not impossible to develop a deterministic alignment procedure taking this deviation into account. For this the objective has to be aligned in its optimum position with the help of directly measuring the PSF. Then, the position of the tube mirror's backreflection should be recorded as well as the rotation angle of the objective. As soon as the objective is used for imaging at high-resolution such an alignment could get necessary.

4.1.3 Examination of the trap focus

For the microtrap the focus shape and size are essential. The test setup provided the possibility to directly examine the created focus which is very difficult in the experimental setup. At the same time sensitivities of the optical trail on the focus shape and eventual limitations could be explored.

In general the size of a focus depends on the numerical aperture and the wavelength of the light λ in the following way

$$w_0 = K \frac{\lambda}{2NA} \, , \tag{4.2}$$

with K parametrizing the illumination of the aperture (for homogeneous illumination $K = 0.82$). In case of focusing a Gaussian beam of a waist w_{ap} clipped by an aperture of radius r_{ap}, the change in focus size can be described by the truncation ratio $T = w_{\mathrm{ap}}/r_{\mathrm{ap}}$ that affects the value of K [CVI]:

$$K(T) = 0.82 + \frac{0.32}{(T - 0.28)^{1.82}} - \frac{0.27}{(T - 0.28)^{1.89}} \tag{4.3}$$

We measured the focus by imaging it with a commercially available microscope objective (Melles Griot, $r = 0.92(10)\,\mu\mathrm{m}$ at $1064\,\mathrm{nm}$) with a magnification of $M \approx 40$ onto a CMOS camera (Guppy F503, pixel size $2.2\,\mu\mathrm{m}$). For a collimated beam with a wavefront errors $< \lambda/4$, a waist of $9.95\,\mathrm{mm}$ and an objective aperture diameter of $24.4\,\mathrm{mm}$ the calculated focus size is $0.88\,\mu\mathrm{m}$ according to equation (4.2). However, we measure a size of about $1.1(1)\,\mu\mathrm{m}$. The aspect ratio an optical trap created with a Gaussian beam with this waist is $\eta = 4.6$ in harmonic approximation. For a beam waist of $15\,\mathrm{mm}$ we expect $0.82\,\mu\mathrm{m}$ and find $0.95\,\mu\mathrm{m}$. This clearly shows that the performance of the objective is not at its nominal values.

If one is again interested in studying quasi-1D physics the aspect ratio η has to be increased. To obtain a more elongated trap the diameter of the Gaussian beam could be decreased. This would require a lot of alignment effort in the later microtrap setup. Another possibility is to truncate the beam by an additional aperture that
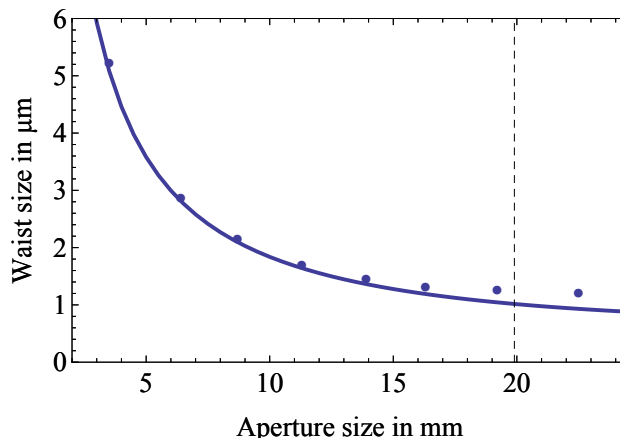
Figure 4.6: Focus size due to beam truncation. The focus is measured for a
gaussian beam of $w_{ap} = 19.9\,\text{mm}$, indicated by the dashed line as a function of
the aperture diameter r_{ap} and compared to the predicted focus according to
equation (4.3) (solid line). The numerical aperture is $\text{NA} = sin(r_{ap}/2f)$ where
$f = 20.3\,\text{mm}$ is the effective focal length of the objective.

is set centrically to the beam. This could cause a rise of the side maxima of the
focus due to diffraction. However, by setting the aperture very far away from the
objective this effect was not very strong. The intensity of the side maxima never
exceeded 15% of the peak intensity. The measured dependence of the waist on the
aperture size is shown in figure 4.6 and compared with the aforementioned relation.
With the given Gaussian beam size the focus waist gets insensitive to aperture sizes
larger than the beam waist. The fact that we measured a beam focus of $1.3\,\text{µm}$ for
open aperture was perhaps due to a trap beam with bad wavefront quality or a not
perfectly centered aperture. For $r_{ap} \approx 10\,\text{mm}$ the focus size reaches the value of the
first generation microtrap.

The focus imaging setup was mounted on a motorized stage (Newport, CONEX-
TRA25CC) and could be moved along the beam axis with high-precision positioning[2].
This allows for the observation of beam profiles of the focus with well-defined relative
distances. Imaging the beam profile slightly before and after the position of the
focus we observed a non-symmetric form. We were able to reduce this asymmetry by
improving the quality of the incident beam. This will be presented in detail in section
4.2.2. However, these features never completely disappeared and partly rotated with
a rotation of the objective.

By focusing also a collimated beam at $671\,\text{nm}$ we could further determine the
chromatic focus shift for the two design wavelenghts of the BA1001 objective to
$15.3(10)\,\text{µm}$. The distance has been measured by the motorized stage.

According to our results from the objective characterization we saw that both
objectives show good but not perfect characteristics compared to the nominal pa-

---

[2]The specifications claim a minimum incremental motion of $0.2\,\text{µm}$ and a guaranteed unidirectional
repeatability of $2\,\text{µm}$.

rameters. Deviations have been observed especially in the resolution measurement and the focus size. We have chosen the objective BA1001 for our setup as its passive alignment led to better results.

4.2 The optical setup

The optical potential created by focusing a collimated beam with the objective serves as a microtrap. A change of the angle of the incidence beam shifts the focus position in the focal plane. This angular tilt is provided by the AOD via deflection, as already illustrated in figure 4.1. A more detailed description of the device and its working principle will be given in section 4.3. The objective and the AOD represent the two key elements of the optical setup for the new microtrap. Furthermore it contains beam shaping and monitor paths for optimal control as well as alignment.

4.2.1 The breadboard for shaping the beam

Due to the new components the optical setup had to be completely redesigned and rebuilt. For the very sensitive high-resolution objective additional alignment tools are necessary. Furthermore, the AOD and the necessary components have to be included in the beam path. The basic setup contains a small collimated beam at 1064 nm that incidents an AOD. The deflected beam is expanded by a telescope and then focused with the objective.

Figure 4.7 illustrates the layout in detail. The infrared beam exits the fiber and is collimated to a waist of 1.23 mm [Kli12]. For polarization cleaning it passes a half wave plate and a polarizing beam splitter cube (PBS). A pellicle beamsplitter extracts a small but fixed proportion of intensity of the beam for power stabilization before the AOD. Then, the beam enters the acousto-optic deflector where it is deflected with an angle depending on the frequency of the applied radio frequency signal. Positioned at a distance of its focal length $f = 18.5$ mm an aspheric lens transfers the angular deviation to a parallel beam shift. A movable aperture mounted together with the spherical lens blocks the redundant deflection orders. A second lens with $f = 300$ mm completes the telescope for the beam expansion to a waist of approximately 19.9 mm. Three mirrors in the telescope allow the alignment of the beam's incident angle and position on the second lens. A subsequent beam sampler extracts a part of the expanded beam for monitoring. For this, the beam is focused by a $f = 500$ mm lens onto a CCD camera (PointGrey, FL3-GE-13S2C-C). It can be used to monitor the configuration of the foci created by the AOD in the intermediate focal plane. Furthermore, the beam profile is monitored by a beam profile camera (WinCam) with a lens of $f = -75$ mm. This camera together with the beam sampler and the reference mirror is part of a Michelson interferometer for the objective alignment. After the beam sampler the main part of the trapping beam passes a non-polarizing beam splitter (NPBS) that reflects 50% of the power through a lens onto a photodiode. The signal is used to stabilize the microtrap beam power.
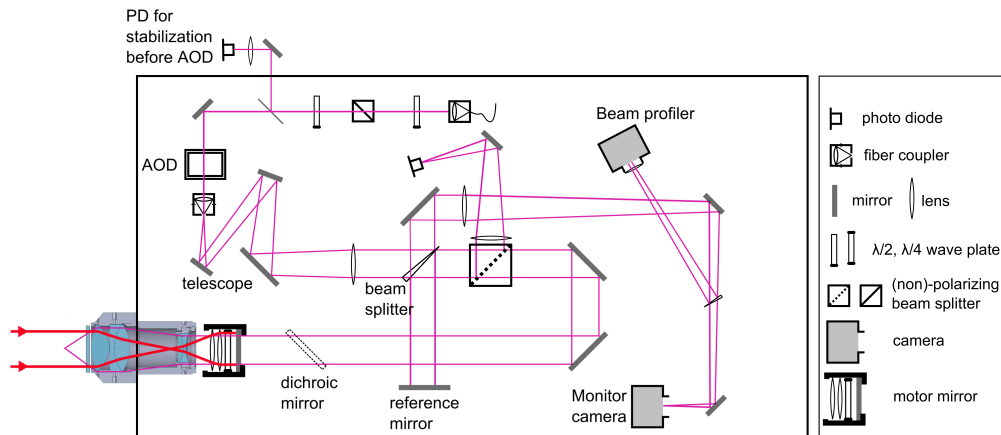
Figure 4.7: Layout of the new microtrap setup. It contains the AOD and the objective as well as an interferometer, power stabilization and monitoring paths.

The transmitted beam passes a dichroic mirror, reflective at 671 nm and mounted in an angle of 45°. The trap beam enters the objective at the end of the breadboard where it is focused through the vacuum window into the chamber.

The objective is mounted 2 mm above the chamber's upper reentrant viewport. Through this vacuum window, the vertical beam for the magneto-optical trap has to be retro-reflected for the MOT loading sequence. The collimated MOT beam which passes the objective from below exits at the top as a diverging beam. Just above the objective the beam is collimated with a lens, traverses a quarter wave plate and hits a mirror where it is retro-reflected. The reflected beam passes the objective again and enters the chamber as a collimated beam. Therefore, although the objective is present the MOT can load. However, the mirror would block the microtrap beam. Therefore, it can be moved out of the beam by a servo motor 2 seconds before the microtrap is required.

For the detection in the MicroMOT, both the microtrap and the MOT have to be functional. The MOT beam is therefore reflected by the dichroic mirror onto a 2-" retro-reflector system[3]. Due to the large divergence angle of the MOT beam and the long distance to the retro-reflector, the final MicroMOT beam diameter amounts to only 1.5 mm which is sufficient to recapture the cold atoms released from the microtrap.

The performance of the objective is very sensitive to the exact alignment with respect to the vacuum window and to the incident beam, as already shown in section 4.1. For this alignment procedure the aforementioned interferometer is used. The reference mirror is mounted such that it is hit perpendicularly by the incident light from the beam sampler. With its help the backreflected beam from the aligned objects can be superimposed with the incident one with high precision by minimizing the fringes of the interference on the camera. Consequently the objective is hit by the beam in the same angle as the reference mirror.

---

[3]again consisting of a convex lens, a quarter wave plate (1.5" diameter) and a mirror

In a first step the incident beam is aligned such that it hits the vacuum window centrally and perpendicularly by minimizing the number of fringes on the camera[4]. Then the objective is installed and a dielectric mirror is laid on its case. Hereby, the objective should be aligned perpendicularly to the incident beam, as well. Note that we have observed in section 4.1 that the reference plane for the objective does not coincide with the lens plane of the objective. Thus it is to be expected that the nominal parameters cannot be achieved by this alignment method.

Another source of wavefront errors is the vacuum window in the reentrant viewport. It has a wedge of about 1.5 ' and can thereby degrade the focus of the microtrap. Additionally its thickness has a tolerance of 0.1 mm. The combined change in rms optical path difference and the resulting wavefront error amount to $\lambda/10$. This has to be added to the error of the objective itself.

4.2.2 Diagnostics of the trap beam

In section 4.1.3 we have seen that the quality of the focus is very sensitive to wavefront errors of the objective. A perfect objective transfers the plane wavefronts of a collimated beam into spherical wavefronts resulting in a small and symmetric focus. It immediately gets clear that the focus quality is also influenced by the incident beam. As soon as it deviates from spherical wavefronts or from plane wavefronts in the limit of perfectly collimation the focus gets asymmetric and larger. The most common components of wavefront error apart from defocusing are third-order aberrations like astigmatisms, comas and spherical. For quantifying these components we need a diagnostic tool that makes the wavefront distortions of the beam measurable.

We use a wedged, lateral shear plate interferometer that usually also serves for beam collimation [Bat47, Mur64]. By hitting a glass plate at a certain angle the incident beam is divided into two components with similar power, as shown in figure 4.8. Due to the different optical path lengths these two components are shifted with respect to each other and their overlap results in an interference pattern [Ril77, Swe90]. The device compares the wavefront at two different spatial positions possible due to a finite shift by the lateral shear. This can be understood as a finite derivative of the wavefront in the direction of the shear and thus delivers information about the wavefront curvature. The resulting interference pattern is projected on a diffuser plate which also provides a reference line.

A collimated beam without abberations results in an interference pattern of straight fringes parallel to the reference line. Any defocusing, i. e. a beam with finite curvature radius in the shear direction causes the fringes to be tilted. By counting

---

[4]The vacuum window is anti-reflection coated for both design wavelengths. So the reflected part of the trapping beam is barely visible and also the interference contrast on the camera is low. For a pre-alignment we implemented a green laser beam (532 nm, 1 mm diameter) and overlapped it with the large infrared beam with the help of two cameras. Then we aligned the setup for the back reflection of the green beam. Switching back to the infrared beam the hardly visible interference on the WinCam was optimized.
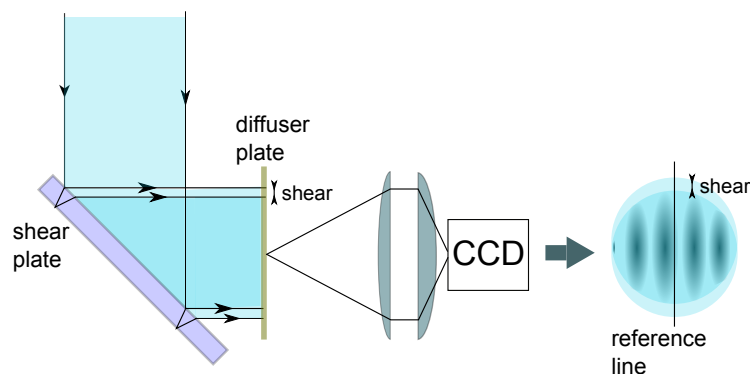
Figure 4.8: Scheme of the lateral shear plate interferometer. The incident beam is divided into two parts with same power that interfere on a diffuser plate with a reference line. A telescope images the pattern onto a CCD camera. The fringes are a measure of the beam's wave front curvature.

the tilted fringes crossing the reference line one can deduce the optical path difference in wavelength between the center and the edge of the beam. Exploiting this the curvature radius in one direction of the incident beam is detectable. For beam curvatures deviating from the spherical form the fringes start to bend. Spherical abberations, e. g., result in s-like fringe forms whereas coma can cause u-formed fringes.

To distinguish the different abberation types and do a full analysis of the beam the interference pattern has to be detected at least in two different axis directions [Swe90]. This allows for a distinction between a global defocus and an astigmatism of the beam. Therefore the shear interferometer is fixed on a rotatable mount. With the information from the shearing interferometer at hand it is not only possible to detect wavefront errors but also to align the components in the optical path[5].

For the beam diagnostics we use a commercially available shear plate interferometer (Thorlabs, SI254). Incident with an angle of 45° on a glass plate out of UV fused silica with a wedge of 18 arcsec and a thickness of 6.35 mm the interference pattern consists of three to four interference fringes for an almost collimated beam with 19.9 mm diameter. The interference pattern projection on the diffuser plate with the reference line is detected with a CCD camera (Thorlabs beam profiler, BC106-VIS) using a 5:1 telescope, see figure 4.8.

The most critical element in the optical train concerning wavefront errors is the aspheric lens right behind the acousto-optic deflector. If it is not hit perpendicularly it will cause an astigmatism of the beam. If it is in addition hit off-center other errors like coma also can appear. It is thus necessary to exactly align the beam to the lens. The same wavefront errors can be caused by the second lens in the telescope. However, its position is not as sensitive to the wavefront due to the large focal length.

With an alignment minimizing the wavefront errors of the beam we were able to

---

[5]The exact alignment procedure of the entire microtrap setup can be found in the section A.
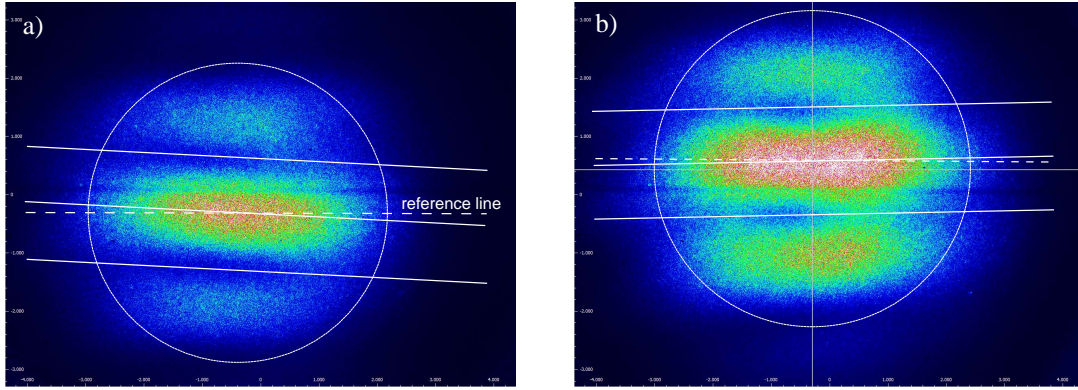
Figure 4.9: Interferograms of the trapping beam taken with a lateral shear plate. (a) horizontal beam direction, (b) vertical beam direction. The dashed lines are parallel to the reference lines. The solid lines interpolate the tilt of the interference fringes. The phase shift of the wavefronts are $< \lambda/8$ over the beam size in both directions. The total astigmatism is smaller than $\lambda/6$.

reduce the initial distortions of $\approx \lambda$ to values smaller than $\lambda/6$. This can be read off the depicted interference patterns in figure 4.9. The visible wavefront error is mainly an astigmatism. This method delivers a quantitative measure of the trapping beam quality.

With this tool at hand we improved the alignment of the optical train creating the microtrap. With minimization of the wavefront errors in the beam we can fully exploit the performance of the high-resolution objective. This is promising for the preparation of atoms in the new microtrap.

4.3 The acousto-optic deflector

The acousto-optic deflector (AOD) represents the second key element of the new microtrap setup. It is supposed to create multiple-well potentials that are well-controllable in their depth and separation.

The working principle is based on the acousto-optic effect. With a piezo-electric transducer density waves are induced in the AOD crystal that act like a grating and partially deflect the transmitted beam. The density waves are created by a radio frequency signal. Its power influences the deflection efficiency of the beam. The frequency translates into the deflection angle. Via a lens an angular deviation translates into a position shift of the focus.

In our setup we use a two-axis acousto-optic deflector (A2D-404AH4, IntraAction Corp.) out of dense flint glass through which the not yet expanded trapping beam is fed. It deflects light at radio frequencies between 25 MHz and 55 MHz and is impedance matched for a center frequency of 40 MHz. Its deflection angle amounts to 2.9 mrad per 10 MHz. This leads to a spatial displacement of 10.6 µm in the focal plane of the objective over the possible frequency range [Kli12] being consistent with
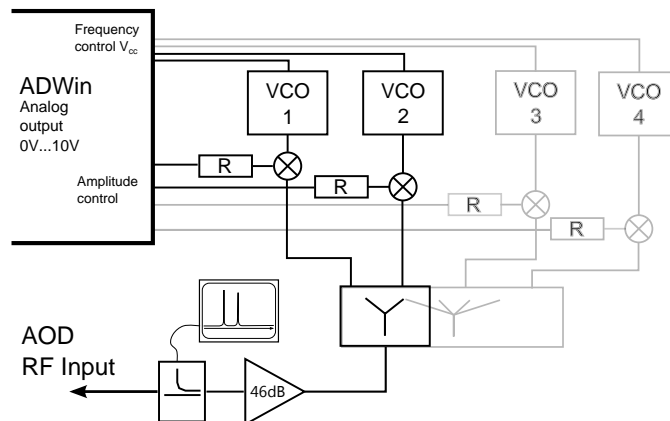
Figure 4.10: Creating a multiple potential landscape. The radio-frequency signal is generated by a voltage-controlled oscillator and variably attenuated by mixing with a controllable DC-voltage. For the creation of the double-well two such branches are combined with a splitter. The signal is then amplified and fed through a coupler for monitoring before it is applied to the AOD. This scheme can easily be expanded by adding further frequency generating components.

the calculation from [Fö05]. This range corresponds to about 9 focus waists.

The potential well depth of a single optical trap depends on the optical light power and thus on the power of the deflected beam. Keeping the beam power going into the AOD constant, the deflected beam power is determined by the diffraction efficiency which varies over the frequency bandwidth and over the radio-frequency amplitude. In addition, the impedance is not matched for the whole radio-frequency bandwidth. This results in a complex effective diffraction efficiency of the beam. The measured diffraction characteristics for both axis of the device is presented in [Kli12]. It has been measured by stabilizing the beam power that enters the AOD and by recording the power of the diffracted beam as a function of frequency and of the attenuation of the rf signal with which we control the AOD.

4.3.1 RF Setup for creating a double-well potential

Applying more than one radio frequency on the AOD causes the initial beam to be deflected in different angles executing more than one deflected beam. This results in multiple-potential wells in the focal plane of the objective. Via the radio frequency signals each well can be controlled and tuned individually concerning its depth and position in the focal plane. The most simple configuration to start with is the creation of a double-well potential. It allows to get experience in the opportunities and limitations of such a configuration. This is also done by investigating the tunneling of atoms between the two wells.

For creating two deflected beams two sources of radio frequency are required at one of the AOD axes. The radio frequencies are produced by commercially available rf components. The exact scheme is depicted in figure 4.10 and designed for simple

control via analog voltages provided by the experiment control system (ADWin). The frequencies are created by voltage controlled oscillators (VCO, MiniCircuits, ZOS-50+) and attenuated by mixing (MiniCircuits, ZX05-5-S+) with a DC voltage. The resulting frequencies are combined in a reversely used splitter (ZFSC-2-1-S+) and amplified by 46 dB (ZHL-5W-1X). With a coupler (ZFBDC20-61HP) right before the radio-frequency input on the AOD we can monitor the created frequencies and observe the respective powers that must not exceed 4 W in total.

For a clear investigation of the physical phenomena in the double well a key concern of the radio-frequency setup is the signal stability. Unfortunately the individual well depths cannot be stabilized via a feed-back loop[6]. So the relative stability has to be characterized. It amounted to about 1 ‰. Details can be found in [Kli12]. This seems to be sufficiently stable for performing precise experiment as we will note in section 5.3.

Starting from controlling the double-well system, the setup can easily be expanded to more wells in a row or to a two-by-two array of wells with individual control. It thus may open the way to investigate few-site Fermi-Hubbard physics.

## 4.4 Implementation of the new microtrap setup into the experiment

The testing of the objective and the characterization of all the elements for the new microtrap provided good results. This encouraged us to implement the new setup into the experiment.

As already mentioned the high-resolution objective has been designed for large numerical aperture and a focal length of 20.3 mm. Therefore, the optical device has to be large in diameter and mounted closely to the vacuum window. Figure 4.11 illustrates the space requirements of the setup. Besides the objective the reentrant viewport contains the Feshbach coils. They had to be replaced by a pair of new coils with adapted dimensions. The basic layout of the coils and the winding number, however, stayed unchanged and can be found in section 3.1.4 or in [Zü09]. The replacement of the coils gave us the opportunity to extend the scheme for the magnetic field stabilization. In a next step the objective could be implemented and the microtrap was superimposed with the dipole trap.

In section 4.4.1 the implementation of the Feshbach coils and the extension of the current control scheme is described. Section 4.4.2 presents the way to superimpose the small-volume microtrap with the optical dipole trap.

---

[6]Reading out the intensity of the well on the CCD is too slow and too unprecise for an active feed-back.
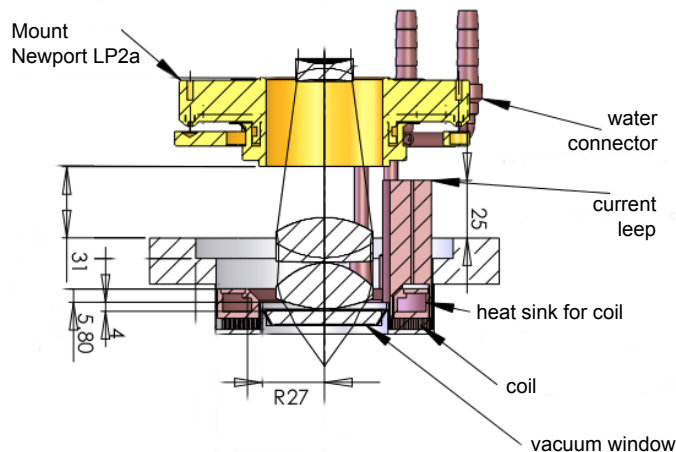
Figure 4.11: The objective in the reentrant viewport. The five-axis mount (Newport LP2a) allows for the alignment of the objective, depicted with its lens configuration, in the reentrant viewport. The objective is mounted close to the vacuum window. The Feshbach coils are placed around the vacuum window guaranteeing high optical access and at the same time being close to the atomic sample.

4.4.1 New Feshbach coils for the experiment

To control the strength of the inter-particle interaction via Feshbach resonances during the experimental sequence the Feshbach coils create a magnetic offset field. In the phase of the sequence where we spill the atoms out of the microtrap the magnetic field gradient is applied by the MOT coils. Unfortunately, they can only provide a rather small gradient due to the larger distance to the atoms. In addition the relatively high inductance leads to a slow ramp speed. To overcome this disadvantage we developed a scheme to create the magnetic offset field and the gradient by the Feshbach coils at the same time, as proposed in [Zü09]. The replacement of the Feshbach coils gave us the opportunity to implement that scheme.

The basic idea, illustrated in figure 4.12 is to use two separate power supplies (SM15-400, Delta Elektronika) that deliver the currents I_1 and I_2 for the two coils. Each of them can deliver a maximum of 400 A and is driven via remote control from the experimental control system ADWin. If they deliver the same current the created field will be a pure offset (gradient) field for Helmholtz (anti-Helmholtz) configuration. Delivering different currents results in a superposition of offset and gradient field.

From the desired gradient and offset field values we can easily deduce the corresponding currents I_1 and I_2 for the coils. For active current feed-back we measure the current difference ($\Delta = I_1 - I_2$) that is proportial to the gradient field and the current sum ($\Sigma = I_1 + I_2$) proportional to the offset field via two current transducers (Danfysik 866 and LEM IT1000). They are stabilized via two digital feed-back loops
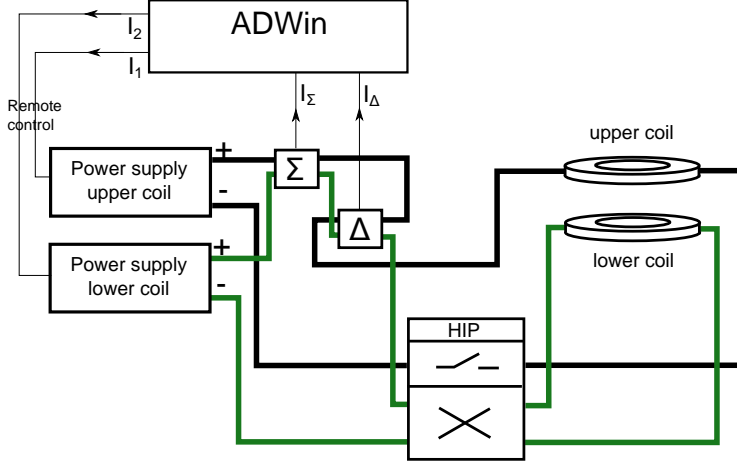
Figure 4.12: Current control scheme of the Feshbach coils. Two separate power supplies are driving the two Feshbach coils independently. Thus, offset fields can be created together with an additional gradient fields using only the Feshbach coil pair. The currents are measured via current transducers detecting the sum and the difference of the currents. Therewith the ADWin stabilizes the magnetic field by corresponding feed-back onto the power supplies.

implemented in the ADWin which produce the signals for the remote control of each power supply. As the two feed-back loops are coupled an important issue is to avoid an oscillation in the control voltages. We managed to implement the stable feedback loop by a proper choice of the loop parameters and at the same time achieved a response time of $2\,\mathrm{ms}$ for driven current steps of $25\,\mathrm{A}$.

For the calibration of the gradient field created by the coils we compensate gravity with a gradient in the Feshbach coils. The required gradient corresponds to $-34.2(2)\,\mathrm{mV}$ in the current transducer Δ. From this calibration we obtain that $1\,\mathrm{V}$ at the analog input of the ADWin corresponds to $32.70(2)\,\mathrm{G/cm}$.

With the newly implemented scheme we are able to apply a magnetic field offset of approximately $1100\,\mathrm{G}$ and still add a field gradient of up to $130\,\mathrm{G/cm}$. So, especially at intermediate offset fields we are very flexible in the choice and the ramp speed of the magnetic field gradient. This will be important for preparation and spilling of the microtrap.

Once the Feshbach coils are implemented in the reentrant viewport further alignment is necessary. Placed slightly further appart than Helmholtz configuration the coils produce a confining magnetic field saddle in the radial plane, as already mentioned in section 3.1.4. This saddle has to be overlapped with the optical dipole trap because in the direction of the weak confinement of the dipole trap the magnetic field saddle can affect the position of the atoms as a function of the magnetic field strength. The shifting of the saddle was done by monitoring the detected escape direction of a small and cold BEC after release and by adding small pieces of steel to the coil. The exact procedure can be read in [Lom11].
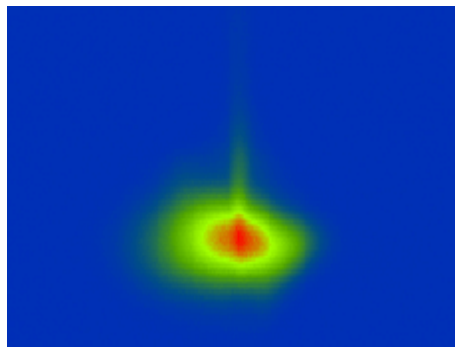
Figure 4.13: A resonant beam passing the magneto-optical trap and scattering off atoms. Assuming that the center of the objective axis coincides with the position of the resonant beam we could localize and align the objective with respect to the dipole trap, getting a reliable starting point for the overlap of the microtrap with the dipole trap. Picture taken with Guppy camera.

4.4.2 Superimposing the microtrap with the dipole trap

After the installation and alignment of the new Feshbach coils, the objective was mounted and interferometrically aligned. It creates the microtrap with a size of about $1 \times 1 \times 5 \mu m^3$ that has to be superimposed with the $10 \times 10 \times 100 \mu m^3$ large dipole trap located in the center of the octagon vacuum chamber with an estimated uncertainty of 2 mm. The superposition of the two optical traps is challenging. We can only detect the microtrap position if it contains atoms. But this means that atoms already have to be transfered from the dipole trap by spatial overlap.

For the overlap with the dipole trap the alignment of the objective in x, y and z direction has to be feasible with a micrometer precision. The objective in the reentrant viewport is mounted in a five-axis lens positioner (Newport, LP-2A) as illustrated in figure 4.11 b. It allows for independent positioning in the two axes of the focal plane (x and y), an angle tilt via two additional screws and adjustment in direction of the beam axis z without rotating the objective itself. We align the objective centrically to the viewport. To get a reference in z-direction a 0.5 mm thin ring made out of PVC is put on the vacuum window and the objective is moved downwards until it touches the ring. Starting from this reference it is moved upwards by about 1.5 mm to the design distance.

With no other tool at hand we would now have to scan a volume of $8 \, \mathrm{mm}^3$ in steps of 10 µm in each directions until we could see an impact of the microtrap on the dipole trap image. This is a rather time-demanding task and so we tried to find out the objective position with respect to the dipole trap in a different way.

The exact position of the dipole trap can be determined by in-situ absorption imaging from two different directions onto two CCD cameras. The detailed imaging scheme is illustrated in figure 3.2. For visualizing the objective's position on the two cameras we used a collimated beam at 671 mm with 1 mm diameter and aligned it very precisely perpendicularly and centrically on the objective. We assumed that
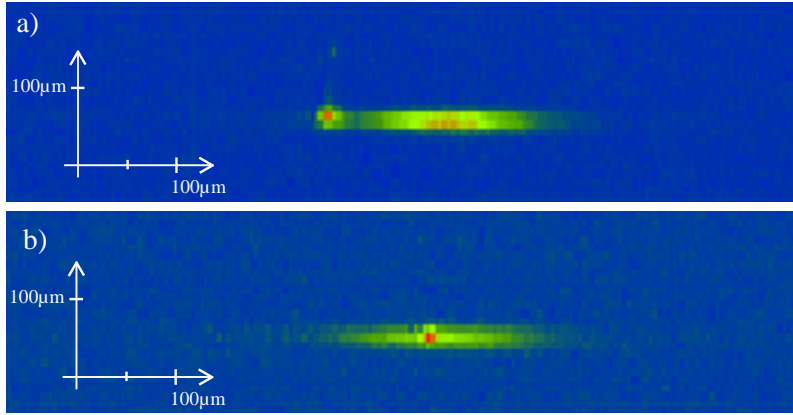
Figure 4.14: Overlap with the dipole trap. (a) shows an absorption image of the dipole trap that is hit by the microtrap beam at the outer left wing. Howeverm in the picture the focus of the microtrap is still above the dipole trap, visible by two pixels with higher amplitude. (b) shows the two traps after the precise superposition. The microtrap sits centrically in the dipole trap in each direction.

the slightly focused resonant beam will be very close to the later microtrap position. In a small magneto-optical trap with low density we wanted to see its impact on the atoms. As shown in figure 4.13 we could observe a beam of atoms scattered out of the sample. It is caused by the resonant photon absorption in one direction and the resulting transfered momentum kicks. By imaging the resonant beam with the two cameras we could map the position of the beam and thus of the objective with respect to the dipole trap. Starting there, we moved the objective in x and y direction until the assumed position of the microtrap coincided with the dipole trap position.

In a next step we loaded atoms into the dipole trap. At the same time the microtrap beam was focused into the vacuum chamber containing an input power of about 200 mW [7]. After altering the height of the objective the impact of the microtrap beam was visible via absorption imaging as an additional small region of higher atom density appearing at the outer wing of the dipole trap, see figure 4.14. The actual microtrap focus was about 50 µm above the dipole trap.

With the microtrap already hitting the dipole trap we started to precisely overlap the two traps. Meanwhile we successively ramped down the power in the microtrap beam as the high atom density in the microtrap leads to atom loss. As the adjustment in the focal plane seemed easy to us and as the trap moves in that plane when adjusting the z-direction, we decided to first align the height of the microtrap to a precision of about 7 µm and shift the dipole trap slighly in vertical direction. Then the overlap in the focal plane was aligned, ending up with the microtrap sitting centrically in the dipole trap as shown in figure 4.14.

For the precise superposition of the two traps in the focal plane of the microtrap

---

[7]Note that this is three orders of magnitude more than the power for the final preparation of our atoms in the microtrap.

we used absorption imaging in vertical direction. The absorption beam hits the atomic cloud from below and the resulting shadow is imaged through the objective and an additional lens onto a CCD camera. As the objective creates the microtrap filled with atoms and also images it onto the CCD camera, the microtrap position recorded on the camera will not change when the position of the objective is changed. For the overlap the dipole trap has to be shifted to the microtrap position. This fact is very useful in order to re-align the microtrap after a complete removal and re-installation of the objective. If nothing in the imaging path except the objective is changed, the two traps are automatically overlapped if the dipole trap position coincides with the former microtrap position on the camera.

Chapter 5

# Few-fermion systems created with the new microtrap setup

After testing and integrating the new setup with the high-resolution objective and the acousto-optic deflector into the experiment we characterized the properties of the new microtrap. We first implemented our deterministic preparation scheme and the detection of few-atom samples. The results will be presented in section 5.1. After this we measured the trap frequencies to gain information about the shape of the optical potential. From the measurement, described in section 5.2, we can infer the focus size and compare it with the results from the direct focus-size measurement described in the previous chapter.

In a next step we used the acousto-optic deflector to create a double-well potential. We prepared a pair of atoms on one site of the double well and measured the evolution of the system. The detailed scheme of the preparation system and the detection of the atom number per well is explained in section 5.3.1. We could observe and control coherent tunneling of the atoms between the two wells presented in section 5.3.2 which demonstrates our high level of control of the system.

5.1 Deterministic preparation revisited

To deterministically prepare samples of few atoms in the new microtrap we use the same preparation technique as presented in section 3.2. However, with the high-resolution objective we expect a smaller trap focus and thus a larger level spacing in the microtrap. This may result in a higher atom number preparation fidelity.

To find the spill parameters for highest atom number preparation fidelity we start by loading about 450 atoms from the shallow crossed-beam optical dipole trap into the microtrap. We then apply a magnetic field gradient of $B' = 31\,\mathrm{G/cm}$ created by the Feshbach coils which reduces the atom number to about 50 atoms. To further reduce the trap depth, the power in the optical trap is reduced from its initial value of $393\,\mathrm{\mu W}$ (3 V on the power detector) to a lower value V_{spill} within 8 ms. We hold the power for 25 ms at this lower value to allow the unbound atoms to escape from the trap region. Then we ramp the trap potential up to the initial value within another 8 ms. Finally, the remaining atom number is detected via fluorescence imaging in the MicroMOT, as described in section 3.2.3. We repeat this measurement for different
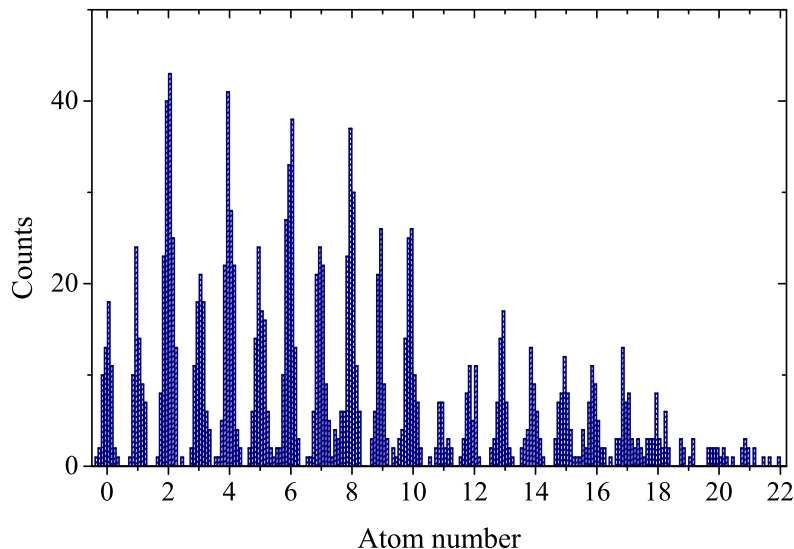
Figure 5.1: Histogram of the measured atom numbers. We detect the prepared atom number by fluorescence imaging in the MicroMOT. The clear peaks separated by $\approx 7\sigma$ are the result of discrete atom numbers.

V_{spill} in order to find the spill levels. Figure 5.1 shows a histogram of the fluorescence signal for all measurements during this run. It shows clear and distinguishable peaks revealing discrete numbers of atoms. For up to 18 atoms the peaks are well separated.

The mean atom number as a function of spill depth is shown in figure 5.2. Starting from zero atoms at $V_{\text{spill}} = 1.8\,\text{V}$ the mean atom number rises with increasing trap depth as more and more atoms stay in the trap. Clear steps of even atom numbers are visible that prove the double occupancy of the trap levels with the two hyperfine states $|1\rangle$ and $|2\rangle$. In between the steps the standard deviation of the mean atom number rises. By setting the spill depth, we can choose how many atoms we want to prepare. However, the plateaus of mean atom numbers are not at integer atom number but slightly lower. This is caused by a non-perfect atom number preparation and detection in the MicroMOT.

Compared to the first-generation microtrap, the new data show much broader plateaus with constant atom number preparation as a function of the trap depth. So, the preparation is less sensitive to instabilities of the trap depth and the spill gradient. This could directly translate to a higher preparation fidelity in the new microtrap due to the reduced focus size of the microtrap. Even for an atom number of 18 we still observe a distinct plateau where we could deterministically prepare our system. This is a factor of two more than we could reach with the old system.

For low trap depth the atom number increases in steps of two atoms. At about 10 atoms the slope of the atom number over trap depth V_{spill} increases. This structure is linked to the trap shape and the resulting occupation of the levels. To illustrate this we assume a cylindrically symmetric harmonic trap with an aspect ratio of $\eta = \omega_\perp/\omega_\parallel = 5$. It is filled with a two-component Fermi gas at zero temperature
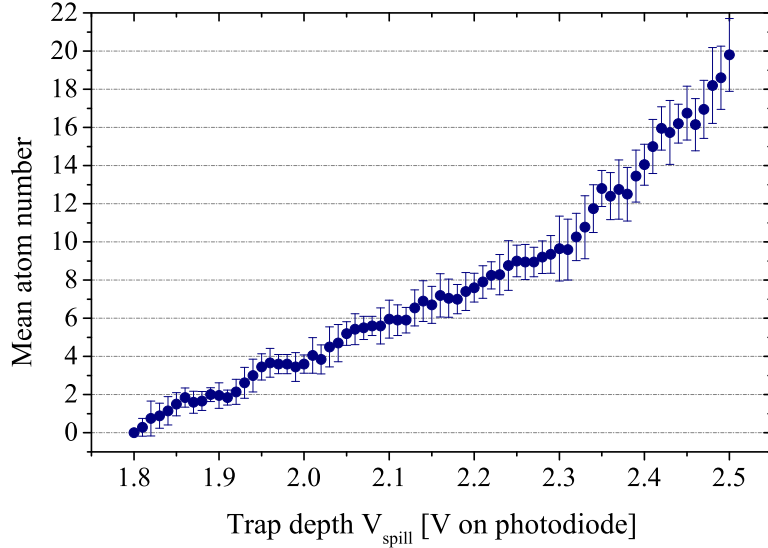
Figure 5.2: Deterministic preparation of a few-atom sample with the new micro-trap setup. By tuning the optical potential depth we can prepare the desired atom number. The clear steps show the possibility of deterministic preparation with a high fidelity due to the reduced trap size. The error bars denote the standard deviation. Due to non-optimal atom number detection the steps are at 90% of the corresponding atom numbers. The structure shows the three dimensional nature of the trap. For up to 10 atoms radial excitations are frozen out and only the axial levels are occupied as we only observe steps with the number of atoms increasing by two. From there on we observe steps of four atoms due to occupations in the radial direction.

where every trap level occupied by two atoms. As the energy differences between the axial levels $\hbar\omega_\parallel$ are smaller the lowest levels occupied by pairs of atoms are only axial excitations. Radially they are in the ground state. Hence, the number of atoms is expected to increase in steps of two. As soon as an energy of $5\hbar\omega_\parallel$ is reached, also the first excited states in the two radial directions can get occupied and the atom number increases by 6 every time the potential depth is increased by $\hbar\omega_\parallel$.

We indeed have such a quasi-harmonic trap, but do not expect an integer aspect ratio and a perfect cylindrically symmetry. Nevertheless, the coarse level structure should be similar when we fill the trap with atoms and spill to a certain point. However, for an atom number larger than 10 the step size does not increase by 6 atoms, as we would expect from our simple picture. This might result from our spilling process that strongly deforms the trap potential. To spill atoms from the trap a magnetic field gradient is applied in the axial direction of the microtrap. Atoms occupying the axial levels experience the deformed potential. In a harmonic three dimensional trap, this deformation in the axial direction has not much effect on the radial directions of the potential. Atoms, populating these states would not be spilled out immediately. Only the anharmonicity of the spilled optical trap couples the radial levels to the axial direction and leads to their depopulation. It might be that the spilling process causes the non-trivial steps in atom number. This has to be investigated in more detail.

Nevertheless, our system allows for a deterministic preparation of few-atom samples. We reach a preparation fidelity of about 80% for two atoms. The deviation from unity preparation fidelity can be caused by non-occupied levels in the system or by a non-perfect recapture into the MicroMOT. The latter possibility seemed more likely to us as the implementation of the objective forced us to reduce the diameter of the MOT beam in vertical direction to about 1.5 mm and the measured distance between the microtrap and the MicroMOT was half this size[1]. Yet, the preparation fidelity is large enough to continue the characterization of the new microtrap.

## 5.2 Characterization of the new microtrap potential

The shape of the optical trap determines the size of the particles' spatial wave functions. The knowledge of the trap shape is thus essential to estimate, e. g., tunneling times of our future systems and to compare the measured values with the theoretical prediction.

A trap characterization by direct imaging of the trap focus is not possible. We can also not expect the same waist size as investigated during the test of the high-resolution objective in section 4.1 where we used a high-quality vacuum window.

---

[1]After the measurements presented in this thesis, we minimized the distance between the microtrap and the MicroMOT. The resulting preparation fidelity of 95% for two atoms confirmed that the recapture was not at its optimum before. The measurement results are presented in the appendix, see B
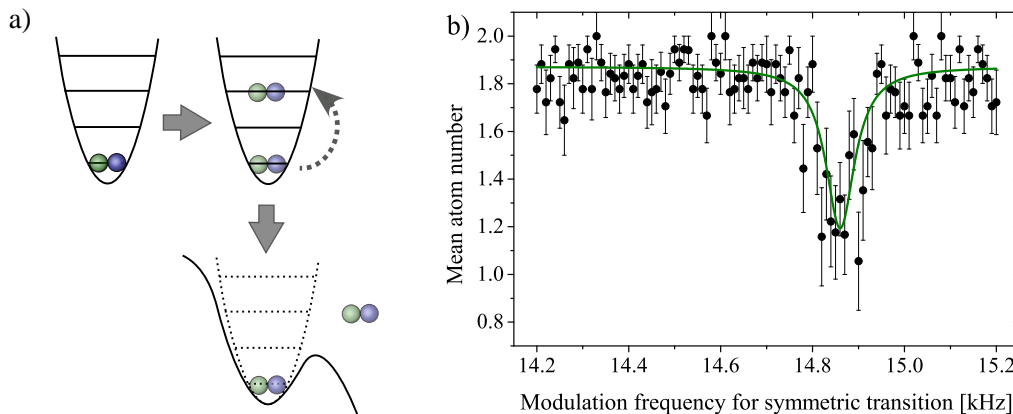
Figure 5.3: Parametric heating to determine the trap frequencies. (a) illustrates the method of parametric heating and subsequent detection to determine the trap frequencies. Two atoms are prepared in the ground state of the trap. Subsequently, it is modulated by a frequency $\omega/2\pi$. If the frequency is equal to a multiple of the trap frequency atoms are transfered to higher levels. By spilling we detect the remaining atoms in the ground state. (b) shows the measurement result for a symmetric trap modulation. At $\omega/2\pi{=}14.6\,\text{kHz}$ the detected mean atom number is minimal. This frequency corresponds to the energy necessary to transfer atoms from the ground state to the second excited axial level.

However, there is a way to deduce the trap shape. We can measure the energy difference between the lowest trap levels and determine the trap frequencies in radial and axial direction for a certain power of the trapping beam. Then, we are able to determine the aspect ratio of our trap and to calculate the focus waist of the trapping beam.

The difference in energy between the lowest lying trap levels can be measured by transferring atoms from the ground state into higher levels. For this we prepare atoms in the lowest state and modulate the trap with a certain frequency. If this frequency is resonant to a transition into higher energy levels the atoms will be transfered into this state, as depicted in figure 5.3 a. This technique is called parametric heating [Fri98]. In principle we can modulate the trap position or the trap depth. Due to symmetry reasons this leads to an excitation of either an odd or an even number of trap levels, respectively.

For the measurement we prepare two atoms in the ground state of our trap with a fixed depth of $390\,\mu\text{W}$ (cf. figure 5.3 a) and then apply the modulation pulse. We detect the remaining number of atoms in the ground state by a second spill down to the ground state level.

An excitation which couples states of even parity is achieved by modulating the trap power. The trap depth is actively stabilized by a feed-back using an AOM that controls the transmitted light power for the microtrap, see section 3.2. In detail, the feed-back varies the power of the radio-frequency applied to the AOM. For the trap
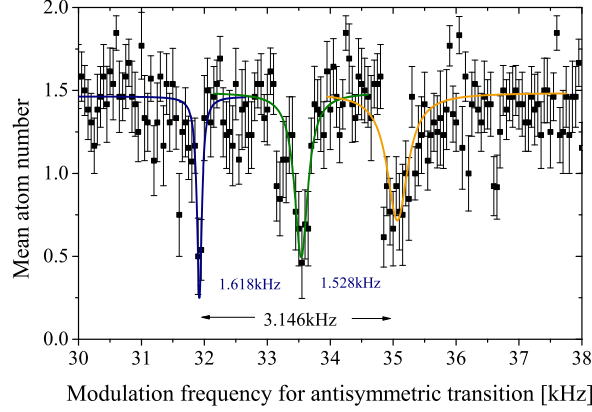
Figure 5.4: Measurement of the radial trap frequencies. The fitted resonances are at $31.921(8)\,$kHz (blue), $33.54(2)\,$kHz (green) and $35.07(4)\,$kHz (yellow). We associate the blue and yellow resonances with the two radial trap frequencies. The central resonance is probably due to a superposition of the other two frequencies. From these measurements we infer the trap focus to be $1.17(6)\,$μm in size assuming a Gaussian beam having the mean radial trap frequency. The error accounts for the uncertainty in the power and the deviation from the mean trap frequency.

frequency measurement an intensity modulation is added to the rf signal and the bandwidth of the feedback loop is set below the modulation frequency.

We have found an excitation signal at $14.860(7)\,$kHz (cf. figure 5.3 b) that we associated with a symmetric transition from the ground state into the second excited axial trap level. Two further resonances, found at about $61(1)\,$kHz and $69(1)\,$kHz (cf. appendix C), correspond to the symmetric transitions into the second excited radial trap levels. As the two radial levels are non-degenerate we conclude that the trap beam has an astigmatism of $\approx 10\%$. A similar value was already found for the first generation microtrap and can at least partly be attributed to the vacuum window.

With the implemented AOD we also have the possibility to move the trap center in the focal plane and excite atoms to a state with different parity. To do this, we modulate the rf-frequency applied to the AOD. Regardless of the modulation direction in the focal plane we see resonances at $31.921(8)\,$kHz, $33.54(2)\,$kHz and $35.07(4)\,$kHz, see figure 5.4. Since they are situated in equal distance we associate the two outer resonances with the radial trap frequencies. This is in agreement with the measured astigmatism of the trap. The central peak may be a superposition of both trap frequencies, but to understand this in detail further investigations are necessary. A detection of the trap frequency in axial direction via the antisymmetric transition into the first excited level was not possible as we can only modulate the center position in radial direction.

With the measurement of the trap frequencies, summarized in table 5.1, we can determine the shape of the trap at a depth of $390\,$μW by assuming a perfect Gaussian beam. A focus waist of $1.17(6)\,$μm can reproduce the mean of the two radial trap

trap direction	transition 0 to 1	transition 0 to 2	anharmonicity
axial $\omega_{\parallel}/2\pi$	not measured	14.860(7) kHz	
radial 1 $\omega_{\perp,1}/2\pi$	31.921(8) kHz	61(1) kHz	4(2)%
radial 2 $\omega_{\perp,2}/2\pi$	35.07(4) kHz	69(1) kHz	2(1)%

Table 5.1: Measured trap frequencies by parametric heating of a prepared two-atom system in the ground state. We are able to transfer the atoms from the ground state to the first and the second excited trap levels. The trap shows an astigmatism of about 10%. The measured aspect ratio of the trap is $\eta \approx 4.5$.

frequencies that we measured. The error accounts for the power uncertainty of 10% and the deviation of the measured trap frequencies from the mean frequency. The calculated aspect ratio for this focus size, using a harmonic approximation is ≈ 5. For the measured aspect ratio we found $\eta \approx 4.5$ which is consistent with the measurement of the atom number as a function of the trap depth in section 5.1.

The new microtrap setup thus represents a significant improvement to the first generation microtrap. The small focus size guarantees a higher preparation fidelity with a lower stability requirement on trap power and the spill gradient.

5.3 Preparation of few-fermion systems in a double-well potential

After we have successfully re-implemented the preparation scheme for low atom numbers in our new microtrap setup we make use of the acousto-optic deflector to create a double-well potential. The control of the tunnel junction of this fundamental system allows us to gain first experiences with multi-well setups. It is a necessary step towards the implementation of few-site Fermi-Hubbard systems.

For the measurement of the tunneling rate between two wells we prepare two non-interacting atoms in one of the two wells whereas the other remains empty. By subsequent lowering of the total trap depth the coherent tunneling process is initialized. We demonstrate the time evolution by measuring the number of particles in one of the two wells after different tunneling times. Tunneling between the two wells is only resonant, when the levels in both wells have the same energy. Furthermore, the process has to occur in accessible time scales. Both, the energy difference of the levels and the tunneling rate are directly controllable by the depth and the separation of the wells.

In this part of the chapter we explain the experimental sequence and the established tools to control a tunnel junction. In section 5.3.1 the preparation of the initial non-tunneling configuration and the detection of the atom numbers in one well are described. In section 5.3.2 we will switch on tunneling between the two wells, fine tune the system and demonstrate Rabi oscillations between the two wells.
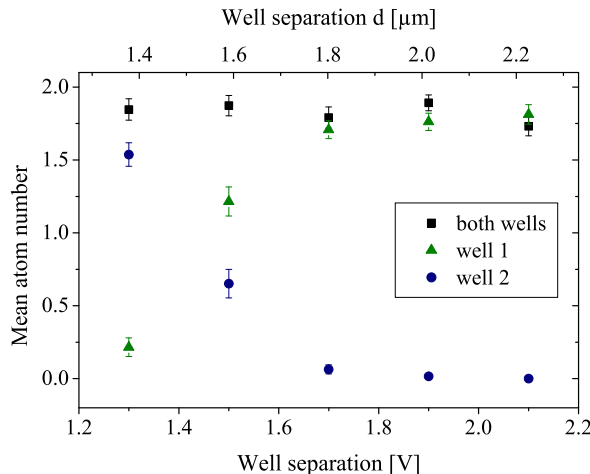
Figure 5.5: Mean atom numbers per well for different well separations at fixed
total trap depth. Two atoms are prepared in well 1. In its vicinity well 2 is
ramped on being slighly deeper than well 1. We detect the atom number in
both wells respectively as function of the separation. For well separations below
1.9 V (about 1.95 µm) a considerable amount of atoms end up in well 2. Above,
the atoms stay in well 1. The total atom number in the system is in agreement
with the initial preparation.

5.3.1 Preparation and detection

Before we can start to investigate tunneling processes we have to deterministically
prepare our system in an initial state. The most convenient possibility is to start
with just one well. Using our usual spilling scheme, we prepare two atoms in the
ground state of the single well (well 1). We ramp on a second well (well 2) within
5 ms with about the same depth. The total double-well trap now contains about
460 µW of trapping light.

For measuring the atom number per site we subsequently separate the two wells
by another 2 µm to completely decouple them. While switching off one of the wells
a small gradient of 10 G/cm is applied to avoid a transfer of atoms into the other
well. The atoms in the remaining well are transfered into the MicroMOT for atom
number detection as it has been done for the single-well microtrap.

The tunneling rate of atoms between the two wells depends on the overall trap
depth P_{tot} and on the well separation d. In our initial configuration we want to
prevent the atoms from tunneling from one well to the other. To find parameters
where tunneling is suppressed, we fix the initial trap depth at 460 µW and search for
the optimal well separation d.

The well separation can be adjusted by the radio-frequency input of the AOD, as
introduced in section 4.3.1. By changing one of the input frequencies (see scheme
4.10), the distance between the wells is varied. Figure 5.5 shows the measurement
result of this variation around a distance deduced from the calculations presented in
[Kli12]. For all separations the total atom number was constant. At large distances all
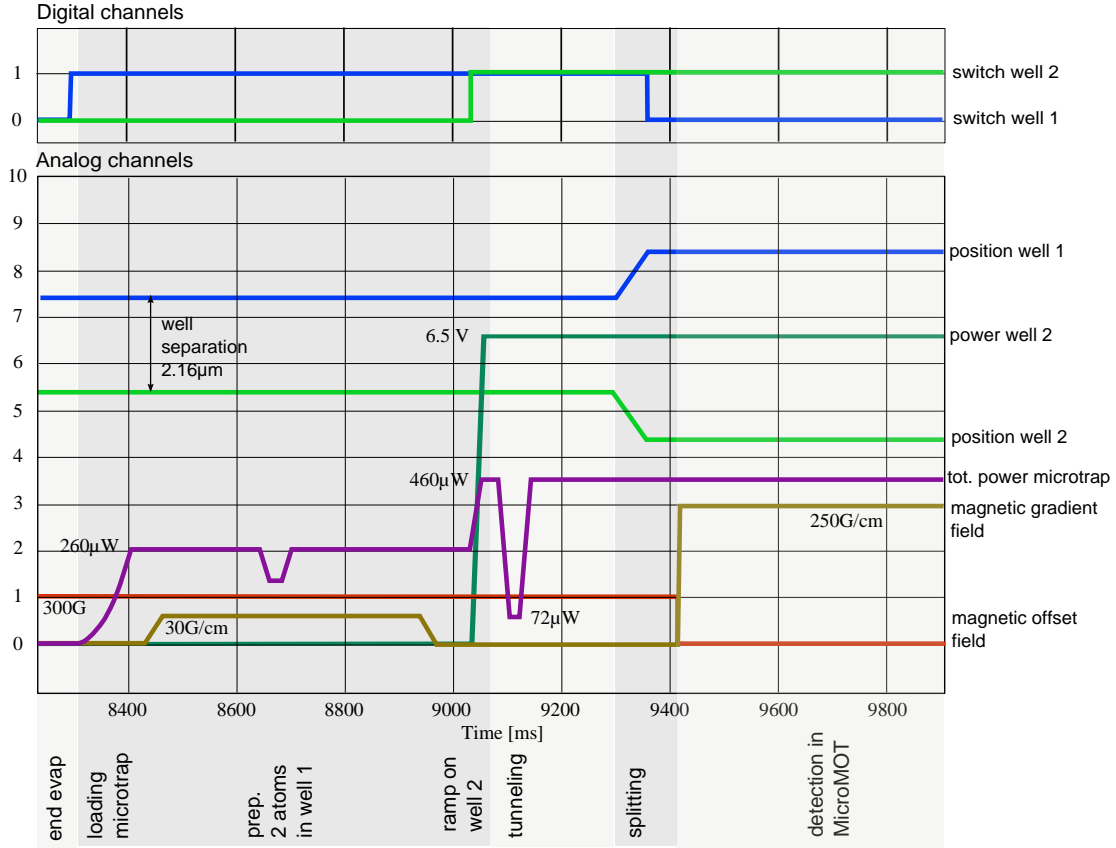
Figure 5.6: Part of the experimental sequence for observing tunneling between two wells. The microtrap is ramped on loading atoms from the dipole trap. With the spilling technique two atoms are prepared in well 1. Then well 2 is ramped on. After a hold time of 30 ms the total trap depth is lowered for a time t_{tunnel} and the atoms can tunnel. By ramping up to the initial total trap depth the tunneling is stopped again. For the detection the two wells are separated in space. Then, well 1 is switched off and the remaining atoms in well 2 are transfered into the MicroMOT for atom counting.

atoms stay in well 1. When we reduce the separation below 1.8 μm (1.7 V difference in the VCO control voltages) the atoms start to tunnel to well 2. Since well 2 was slightly deeper than well 1, the mean atom number in well 2 exceeds 50%. For future measurements we want to start in a system without tunneling. So, we chose an initial well separation of 2.05 V which corresponds to about 2.16 μm.

5.3.2 Observations of tunneling processes

Up to now the prepared systems contain two atoms in well 1. The distance to well 2 is large enough that no tunneling occurs for the chosen trap depth. The next step is to investigate the tunneling dynamics. To start the tunneling process at fixed separation we reduce the trap depth by a factor of 6.4. To observe resonant tunneling
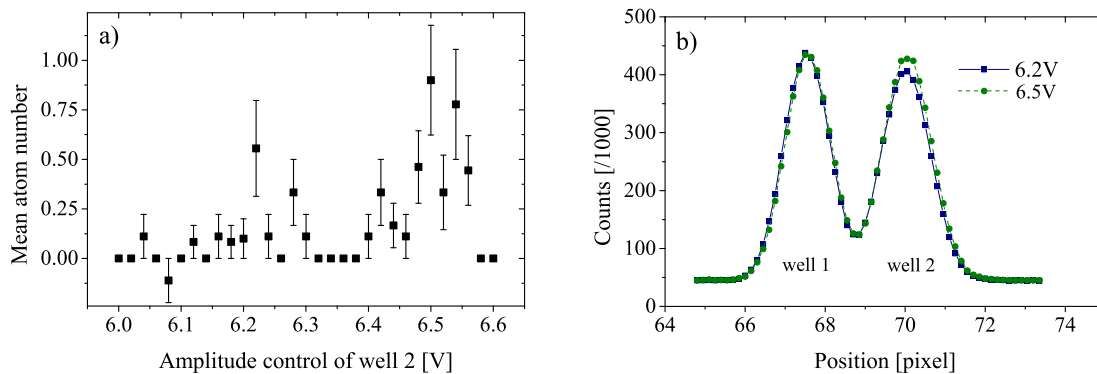
Figure 5.7: Tunneling features as a function of relative well depth. (a) For the tunneling times 20, 25 and 30 ms the population in well 2 has been measured as a function of the relative well depth. For the plot the results for the different tunneling times are averaged. Signatures of tunneling are indicated by an atom number differing from zero and a large standard deviation. Features indicating tunneling are found at 6.2 V and 6.5 V. (b) shows the intensity profile of the trapping light. The double well structure was measured for the values of the two features. For a setting of 6.5 V the wells look equally deep (green, dashed), whereas for 6.2 V well 2 is less deep (blue, solid) than well 1. The lines are a guide to the eye.

the depth of the two wells have to be equal.

The experimental sequence is illustrated in figure 5.6. Again, we prepare two atoms in one well. Subsequently, we ramp on the second well within 20 ms to a well depth similar to that of well 1. The reduced ramp speed should prevent heating of the system. After a hold time of 30 ms, the trap depth of the double well is reduced within 20 ms to a total power of 72 μW and the tunneling process can start. After a certain time t_{tunnel} the evolution is stopped by increasing the trap depth within another 20 ms. Finally, the atom number in well 2 is detected.

To obtain resonant tunneling we have to fine tune the relative well depth. Therefore, we alter the control value of the amplitude of well 2, see scheme 4.10. As the total trap power is stabilized, the variation of the amplitude in well 2 directly leads to a potential tilt δ between the two wells. We measured the atom number in well 2 for three different t_{tunnel} of 20, 25 and 30 ms as a function of the tilt δ. The averaged results for the different t_{tunnel} are shown in figure 5.7 a. We observe two broad features at control values of 6.2 V and 6.5 V where the atom number in well 2 differs from zero and the standard deviation of the mean atom number is large. We assumed this to be a signature of tunneling in the system.

Profiles of the intensity distribution at these control values are shown in figure 5.7 b. For a mixer value of 6.2 V the two wells are not of equal depth. As well 2 is less deep than well 1, the feature can not be explained by a tunneling process into an excited axial level of well 2. To understand this structure further detailed measurements would be necessary.
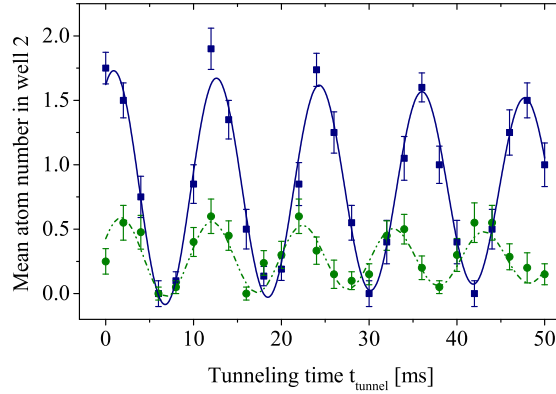
Figure 5.8: Rabi oscillations for two different relative well depths. Starting with two atoms in well 1 the atom number in well 2 is measured as a function of the tunneling time t_{tunnel}. For the fit we assumed a sinusoidal modulation combined with an exponential decay. The blue data is obtained for a mixer value of 6.50 V. Taking into account the 90% recapture efficiency of the MicroMOT, this oscillation with a fitted (blue, solid line) amplitude of 0.92 can be attributed to resonant tunneling. The Rabi frequency is $\Omega = 2\pi \times 85.5(4)$ Hz and the decay time is 180(74) ms. At a mixer value of 6.55 V we observe a reduced oscillation amplitude of only 0.32 and a frequency of $\Omega_{\text{eff}} = 2\pi \times 96.9(11)$ Hz. Also the decay time decreased to 97(59) ms.

For a value of 6.5 V the depths of both wells are nearly equal. We measured the atom number in well 2 for tunneling times between 0 and 50 ms and observed oscillations as shown in figure 5.8. For a mixer value of 6.50 V we see Rabi oscillations (blue data) of the atoms between the two wells with a relative amplitude of 0.92. As our recapture efficiency into the MicroMOT is only about 90% we can assume that the tunneling coupling is resonant. We fit the measured atom number with an exponentially damped sine-square function and obtain a Rabi frequency of $\Omega = 2\pi \times 85.5(4)$ Hz [2]. The decay time due to decoherence is about 180(74) ms. At a second relative well depth of 6.55 V the system is slightly tilted and we measured Rabi oscillations with a smaller amplitude of 0.32 and larger frequency of $\Omega_{\text{eff}} = \sqrt{\Omega^2 + \Delta^2} = 2\pi \times 96.9(11)$ Hz (green data). In comparison with the resonant Rabi frequency, these values are not consistent with the Rabi formula (2.17).

The measured amplitude of the non-resonant oscillation is much lower than the expected values of $\Omega^2/\Omega_{\text{eff}}^2$. One possible explanation is a change in the tunneling rate Ω to smaller values when the potential is tilted, but further investigations thereon are required.

Nevertheless, this first oscillation measurement confirmed that a high level of control is possible with our new setup. A detailed characterization of the Rabi

---

[2]Despite the restriction to only one dimension, the tunneling calculation presented in section 2.3 yields a tunneling rate that is only smaller by a factor of 10 for our experimental parameters of the double-well potential.

oscillations Ω_{eff} as a function of the relative depth δ allows to gain further insight into the properties and stabilities of our system. It provides a sensitive tool to set the depths of two wells to equal heights.

After the investigation of resonant tunneling at a certain separation d and a total trap depth P_{tot}, a future step will be to vary the two parameters and thus alter the time scale of the tunneling process. A full characterization of the tunneling junction $J(d, P_{\text{tot}})$ will give us the opportunity to control the tunneling time scales in later experiments. Together with the tunability of the inter-particle interaction strength, we want to observe ordering phenomena such as the anti-ferromagnetic phase.

Chapter 6

Conclusion and Outlook

During the past two years, our group has used an optical microtrap created by the focus of a single Gaussian laser beam to deterministically prepare and investigate few-fermion systems [Ser11b, Zü12a, Wen13]. In the course of this thesis we have developed, tested and commissioned a new experimental setup which allows to perform such experiments in a tunable potential.

For this setup we have used a high-resolution objective, which was designed by F. Serwane [Ser11a], to decrease the focus size of the microtrap. We characterized the objective by measuring the transmitted wavefront error and the achievable resolution in a test setup and found both to be within the specifications. We also included a two-axis acousto-optic deflector into the new setup that allows the creation of multiple potential wells by deflecting the trapping beam into different orders. Since direct diagnostics of the focus created by the objective are not possible in the experiment we developed an alignment procedure to integrate the new microtrap setup into the existing experiment.

After overlapping the new microtrap with our optical dipole trap and re-establishing the deterministic preparation of few-fermion systems we found the preparation fidelity to be much less sensitive to the depth of the microtrap potential. We attribute this to the smaller size of the trap. We measured the trap frequencies in the different axies of the trap and infered a focus size of $1.17(6)\,\mu m$ which indicates that the new objective works as expected.

As a first test of our ability to tune the potential shape we used the acousto-optic deflector to create a double-well potential. For this we developed a radio-frequency setup with an amplitude stability of the generated radio-frequency signals below $1\,\permil$. In this tunable double-well potential we prepared two non-interacting atoms in one of the wells and observed resonant tunneling to the second well. By adjusting the relative height of the two wells we could create high-contrast oscillations with coherence times of several hundred milliseconds.

Starting from this well controlled and stable system the next step is the deterministic atom number preparation of few-fermion systems in our symmetric double well potential. Here one would start with the simplest possible system, which is two distinguishable fermions in the symmetric ground state of the double-well potential. Our planned preparation scheme for this state is to start from two separate wells, each containing two atoms in the ground state. If we then combine the potential

into a single double-well, the atoms will occupy the symmetric ground state and the anti-symmetric first excited state in the double-well potential. As these states have an energy separation of $2t$ we can then spill the first excited state by applying a magnetic field gradient. Using this scheme we should be able to reliably prepare two atoms in the lowest state of the double well, which corresponds to a Fermi Hubbard system at half filling.

In this system we could then investigate the two-particle-limit of the transition from a metallic to an insulating state by measuring the occupation number of the individual wells. Once we have observed the Mott-insulating regime we can study superexchange correlations in our isolated two-site potential as already demonstrated for bosons [Tro08] and for fermions [Gre13] in double-well superlattices. With the help of the acousto-optic deflector we can then go a step further and extend our system to more than two wells. At low enough entropy these systems should exhibit spin order which we can directly probe by spin-selective measurement of the populations in the different wells. By tuning the Hubbard parameters we should be able to investigate the phase transition to the finite-size anti-ferromagnetic state and compare it with theory predictions [Gor12].

Instead of a chain of potential wells the two-axis acousto-optic deflector also allows for the creation of two-dimensional multiple-well arrays. The simplest configuration is a two-by-two array, shown in [Kli12] which can be considered as an elementary plaquette of a two-dimensional lattice with independent tunability of the tunneling rates in both directions. The AOD may allow the creation of finite 2D lattices with up to 4×4 sites. As the potential depths are indiviually controllable we can also simulate lattice defects affecting the physics in our finite lattice system.

The creation of time-averaged potentials is a completely different technique possible with the AOD. By successively creating single wells at different positions with a repetition rate much faster than the trap frequencies the generation of two-dimensional lattice potentials with arbitrary geometries, e. g. triangular plaquettes should be possible. Furthermore, a continuous modulation allows the deformation of a single well. By exploiting this, we should be able to create a two-dimensional trap and may investigate its shell structure.

All the mentioned examples illustrate the large flexibility of our new setup. The high degree of stability and control we achieved in our first experiments with the double-well potential combined with our improved few-particle preparation makes us confident that we will be able to use this setup to do lots of interesting physics in the near future.

Appendix A

Alignment instruction for the multiwell breadboard

The focus created by the high-resolution objective is sensitive to wavefront errors in the optical system. Thus, after the adjustment of the board to the G-tower a proper alignment of the optical setup on the breadboard is necessary. The AOD, the telescope and the objective itself are the most critical elements to align.

For the AOD a high deflection efficiency in the frequency center is necessary. The telescope can create an astigmatism to the beam if it traverses one of the lenses not centrally or with an angle. The objective has to be adjusted with respect to the vacuum window. For this we align first the incident beam with respect to the window interferometrically. Then we install the objective and align it with respect to the beam.

1. Alignment of the acousto-optic deflector

With no stabilization board in between the Mephisto board and the AFM board about 116 mW of 1064-nm light exit the fiber. For horizontal polarization being maximally transmitted through the cube 106 mW are measured behind the pelecal.

Check first with the IR-viewer whether the beam is not clipped when it crosses the AOD crystal. A total power of about 98 mW should be left behind the crystal.

For the diffraction optimization of the AOD we use the camera (PointGrey) in the diagnostic arm by comparing the power in the four generated spots. Then, block all but the -1-1 order (say 11-order) and optimize with the power meter while checking that you hit the crystal properly. The coupling efficiency should be approximately 8-10% for $A_H = 32.75$dBm at $f_1 = 37.89$ MHz and $A_V = 32.75$dBm at $f_2 = 32.02$ MHz.

The beam should hit the 1/2" mirror behind the small lens in the center. Then also the lens with $f = 18$ mm is traversed centrally. If this is not the case a coarse alignment with the AOD together with the mirror in front has to be done.
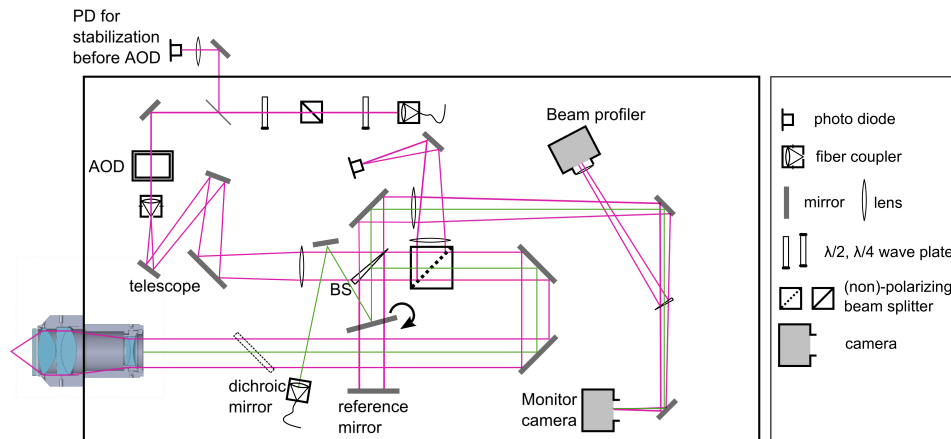
Figure A.1: Optical setup of the new microtrap

2. Telescope

With the help of the 1/2 mirror and the 2" mirror we adjust position and angle of the divergent beam on the 2" lens. The angle can be checked with a retroreflector screwed on the lens mount reflecting back through the AOD and the aperture. For means of collimation and control over the wave fronts, a shearing interferometer is set at the later objective position. Collimation is achieved by altering the position of the 2" lens that is fixed on a rail.

The wavefront curvature has to be small in both the horizonal and vertical axis of the beam. It can be optimized by the alignment of the telescope. If the beam hits the first mirror in the telescope in the center and the AOD diffraction efficiency is optimized one can slightly scan the beam position on the small lens via the mirror in front of the AOD and re-align the telescope as described before. If the beam has significant wavefront errors it is necessary to alter the relative positions of incident beam and AOD more drastically.

3. Interferometer

The Michelson interferometer behind the telescope is necessary to align the objective. Only if the reference arm is aligned such that the beam hits the reference mirror perpendicularly, the objective can be aligned perpendicularly to the beam. To set the position of the reference mirror we first install a second mirror at the position of the later objective. We align it such that light of the 00-order is reflected back through all the optics on the board and fed through the fiber. With this we made shure that the mirror at the objective position is hit perpendicularly by the 00-order.

For the rest of the procedure we use again the 11-order. The reference mirror in the second branch of the interferometer has to be adjusted. Therefore we interfer the beam reflected directly at the beam sampler with the part going straight through it, which is then reflected at the objective mirror, at the beam sampler and at the

reference mirror and traverses the beam sampler. Both beams should overlap and interfere on the WinCam in the diagnostic branch. The angle error due to the two different diffraction orders that we used is approximately 0.5 mrad

4. Green laser

For the alignment of the expanded beam with respect to the antireflection-coated vacuum window we use a green beam at 532 nm that we overlap with the IR-beam. It faciliate the alignment to the center of the window and the angle as the window is anti-reflection coated at 1064 nm and the reflected part of the beam is barely visible.

The overlap of the green laser beam with the IR-beam is done on two cameras, the Point Grey on which the foci have to be at the same position, and a beam profiler camera (Thorlabs) that we install at the position of the objective. As the chip of the latter is fairly large, we are able to see the center of the IR-beam and overlap it with the center of the green beam. The overlap on the PointGrey is aligned with the 1"-mirror, the overlap on the beam profiler is done with the fiber outcoupler of the green laser.

5. Vacuum window

After that the trap beam has to be aligned with respect to the vacuum window. For this the green beam is aligned onto the vacuum window in position and angle via the two large mirrors behind the NBSC. Then one has to search for interference of the reflected IR-beam on the WinCam. The contrast is very small. As soon as little fringes appear at the edge of the beam, one can improve the signal by subtracting the light beam and normalizing the difference picture with the help of the WinCam software.

6. Objective

Before installing the objective onto the breadboard the mount is align such that the objective sits perpendicular in the center. The z-axis screw has to sit at the outer edge of the alignment way such that we have the maximum travel to screw the objective down into the reentrant viewport. We have to find the best position of the objective on the board and the objective case in the mount such that the objective sits as close as possible to the vacuum chamber but we can still access the alignment screws of the 5-axis mount. We have to tighten the in the mount accordingly with the aluminium ring. Then the objective can be installed on the breadboard. To adjust the distance between the vacuum window and the objective, we screw the objective down until it touches a 0.5 mm- thick plastic ring. Starting at this reference position we screw it up by 1.5 mm.

The angular alignment of the objective is done with a 2" dielectric mirror that is layed onto the objective with the coated side downwards. We align it with the interference of the backreflection on the WinCam. The exact position of the objective has to be aligned with respect to the dipole trap. A detailed description is given in section 4.4.2.

Appendix B

Deterministic preparation after improved recapture efficiency into the MicroMOT

After the measurements presented in section 5 of this thesis, the recapture of the atoms from the microtrap into the MicroMOT has been improved by moving the microtrap closer to the MicroMOT position. Then, the system was prepared as presented before. A plot of the mean atom number over the trap depth V_{spill} (cf. figure B.1 a) shows clear steps of two and four atoms with broad plateau regions. Between four and ten atoms, the steps were not clearly visible.

We measured the preparation fidelity of two atoms in the microtrap by choosing a trap depth of $1.58\,\mathrm{V}$. The fluorescence light imaged on the camera (Andor) is integrated over the MOT region. The results are binned into a histogram, see figure B.1 b. In $95(1)\%$ of the experimental realizations, we prepared exactly two atoms. The remaining 5% were realizations of one or zero atoms, but we never obtained more than the wished atom number. From this we conclude that our preparation fidelity is not limited by the stability of the magnetic field gradient or the trap depth. The mispreparations may be caused by a finite detection efficiency or by holes in the Fermi distribution of our prepared sample.
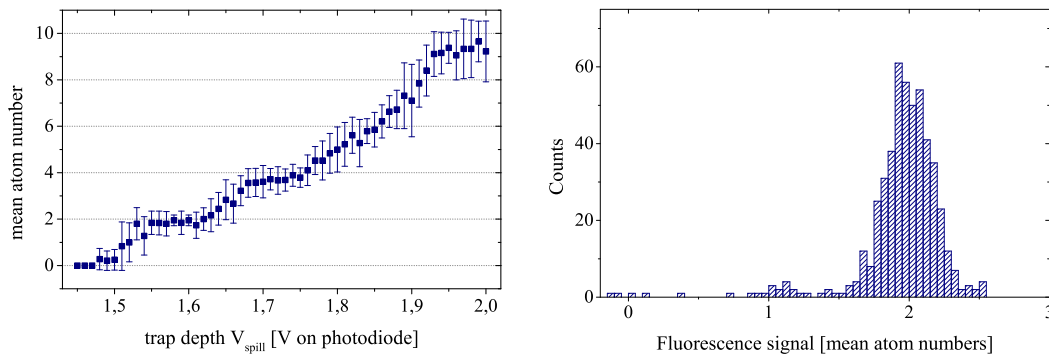
Figure B.1: Preparation fidelity after an improved recapture into the MicroMOT. (a) shows the mean atom number as a function of the trap depth. (b) Histogram of preparation of two atoms.

Appendix C

Trap frequencies in radial direction

By modulating the trap power with a frequency between 60 kHz and 80 kHz we measure the energy difference from the ground state level to the second excited level in the radial direction. We see features at 61(1) kHz and 69(1) kHz which we associate with resonances for parametric heating into the second excited states. Their position and separation are in agreement with the measured trap frequencies in radial direction, shown in figure 5.4.
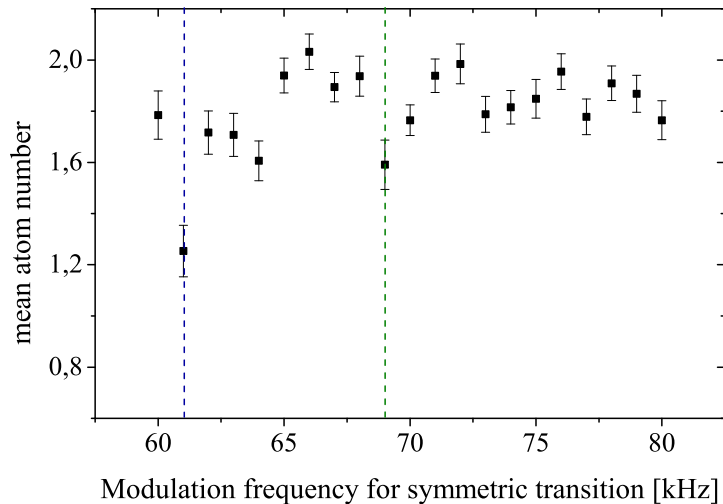
Figure C.1: Parametric heating into the second excited radial level. We observe resonance features at 61(1) kHz and 69(1) kHz which we associate with the population transfer from the ground state level into the second excited radial levels.

Bibliography

[Aha88] A. Aharony, R. Birgeneau, A. Coniglio, M. Kastner, H. Stanley, *Magnetic phase diagram and magnetic pairing in doped La_2CuO_4*, Physical review letters **60**(13), 1330–1333 (1988).

[And59] P. W. Anderson, *New Approach to the Theory of Superexchange Interactions*, Phys. Rev. **115**, 2–13 (Jul 1959).

[And95] M. H. Anderson, J. H. Ensher, M. R. Matthews, C. E. Wieman, E. A. Cornell, *Observation of Bose-Einstein Condensation in a Dilute Atomic Vapor*, Science **269**, 198–201 (1995).

[Bak09] W. S. Bakr, J. I. Gillen, A. Peng, S. Fölling, M. Greiner, *A quantum gas microscope for detecting single atoms in a Hubbard-regime optical lattice*, Nature **462**(7269), 74–77 (2009).

[Bar04] M. Bartenstein, A. Altmeyer, S. Riedl, S. Jochim, C. Chin, J. H. Denschlag, R. Grimm, *Crossover from a molecular Bose-Einstein condensate to a degenerate Fermi gas*, Physical review letters **92**(12), 120401 (2004).

[Bat47] W. Bates, *A wavefront shearing interferometer*, Proceedings of the Physical Society **59**(6), 940 (1947).

[Blo05] I. Bloch, *Ultracold quantum gases in optical lattices*, Nature Physics **1**, 23–30 (2005).

[Chi10] C. Chin, R. Grimm, P. Julienne, E. Tiesinga, *Feshbach Resonances in Ultracold Gases*, Reviews of Modern Physics **82**, 1225 (2010).

[CVI] CVI Melles-Griot, *https://www.cvimellesgriot.com/Products/Documents/ TechnicalGuide/Gaussian-Beam-Optics.pdf*.

[Dal99] J. Dalibard, *Collisional dynamics of ultra-cold atomic gases*, in *Proceedings of the International School of Physics-Enrico Fermi* (1999).

[Dav95] K. B. Davis, M.-O. Mewes, M. R. Andrews, N. J. van Druten, D. S. Durfee, D. M. Kurn, W. Ketterle, *Bose-Einstein Condensation in a Gas of Sodium Atoms*, Phys. Rev. Lett. **75 (22)**, 3969–3974 (1995).

[DeM99] B. DeMarco, D. Jin, *Onset of Fermi degeneracy in a trapped atomic gas*, Science **285**(5434), 1703–1706 (1999).

Bibliography

[DL08]   L. De Leo, C. Kollath, A. Georges, M. Ferrero, O. Parcollet, *Trapping and cooling fermionic atoms into Mott and Néel states*, Physical review letters **101**(21), 210403 (2008).

[Fri98]   S. Friebel, C. D'Andrea, J. Walz, M. Weitz, T. W. Hänsch, *CO_2-laser optical lattice with cold rubidium atoms*, Phys. Rev. A **57**, R20–R23 (Jan 1998).

[Fö05]   J. Fölling, *Bose-Einstein Josephson Tunneling and Generation of Arbitrary Optical Potentials*, Diploma thesis (2005).

[Geh03]   M. E. Gehm, *Properties of 6 Lithium*, Dep. of Physics, DUKE University http://www. phy. duke. edu/research/photon/qoptics/ tech-docs/pdf/PropertiesOfLi.pdf **21** (2003).

[Gor12]   E. Gorelik, D. Rost, T. Paiva, R. Scalettar, A. Klümper, N. Blümer, *Universal probes for antiferromagnetic correlations and entropy in cold fermions on optical lattices*, Physical Review A **85**(6), 061602 (2012).

[Gre13]   D. Greif, T. Uehlinger, G. Jotzu, L. Tarruell, T. Esslinger, *Short-Range Quantum Magnetism of Ultracold Fermions in an Optical Lattice*, Science (2013).

[Gri00]   R. Grimm, M. Weidemüller, Y. B. Ovchinnikov, *Optical Dipole traps for neutral atoms*, Advances in atomic, molecular, and optical physics **42**, 95–170 (2000).

[Hub63]   J. Hubbard, *Electron correlations in narrow energy bands*, Proceedings of the Royal Society of London. Series A. Mathematical and Physical Sciences **276**(1365), 238–257 (1963).

[Ima98]   M. Imada, A. Fujimori, Y. Tokura, *Metal-insulator transitions*, Rev. Mod. Phys. **70**, 1039–1263 (Oct 1998).

[Ino98]   S. Inouye, M. R. Andrews, J. Stenger, H.-J. Miesner, D. M. Stamper-Kurn, W. Ketterle, *Observation of Feshbach resonances in a Bose–Einstein condensate*, Nature **392**, 151–154 (1998).

[Jak98]   D. Jaksch, C. Bruder, J. I. Cirac, C. W. Gardiner, P. Zoller, *Cold bosonic atoms in optical lattices*, Physical Review Letters **81**(15), 3108–3111 (1998).

[Jö08]   R. Jördens, N. Strohmaier, K. Günter, H. Moritz, T. Esslinger, *A Mott insulator of fermionic atoms in an optical lattice*, Nature **455**(7210), 204–207 (2008).

[Jö10]   R. Jördens, L. Tarruell, D. Greif, T. Uehlinger, N. Strohmaier, H. Moritz, T. Esslinger, L. De Leo, C. Kollath, A. Georges, *et al.*, *Quantitative determination of temperature in the approach to magnetic order of ultracold fermions in an optical lattice*, Physical review letters **104**(18), 180401 (2010).

[Kli12]   V. M. Klinkhamer, *An apparatus for few-fermion systems in multiple well potentials*, Masters Thesis, Department of Physics and Astronomy, University of Heidelberg (2012).

[Koe08]   A. Koetsier, R. Duine, I. Bloch, H. Stoof, *Achieving the Néel state in an optical lattice*, Physical Review A **77**(2), 023623 (2008).

[Koh08]   M. Kohnen, *Ultracold Fermi Mixtures in an Optical Dipole Trap*, Diploma thesis (2008).

[Kra34]   H. Kramers, *L'interaction entre les atomes magnétogènes dans un cristal paramagnétique*, Physica **1**, 182–192 (1934).

[Lom11]   T. Lompe, *Efimov Physics in a three-component Fermi gas*, Dissertation, Ruperto-Carola University of Heidelberg (2011).

[Mah82]   V. N. Mahajan, *Strehl ratio for primary aberrations: some analytical results for circular and annular pupils*, JOSA **72**(9), 1258–1266 (1982).

[McK11]   D. McKay, B. DeMarco, *Cooling in strongly correlated optical lattices: prospects and challenges*, Reports on Progress in Physics **74**(5), 054401 (2011).

[Met99]   H. J. Metcalf, P. Van der Straten, *Laser cooling and trapping* (Springer Verlag, 1999).

[Met03]   H. Metcalf, P. van der Straten, *Laser cooling and trapping of atoms*, J. Opt. Soc. Am. B **20**(5), 887–908 (2003).

[Mur64]   M. Murty, *The use of a single plane parallel plate as a lateral shearing interferometer with a visible gas laser source*, Applied Optics **3**(4), 531–534 (1964).

[Nei13]   M. Neidig, *A realization of a two-dimensional Fermi gas in a standing wave trap*, Masters Thesis, Department of Physics and Astronomy, University of Heidelberg (2013).

[Ott06]   T. Ottenstein, *A New Objective for High Resolution Imaging of Bose-Einstein Condensates*, Diploma thesis (2006).

[Ott10]   T. B. Ottenstein, *Few-body physics in ultracold Fermi gases*, Dissertation, Ruperto-Carola University of Heidelberg (2010).

[Ril77]   M. E. Riley, M. A. Gusinow, *Laser beam divergence utilizing a lateral shearing interferometer*, Applied Optics **16**(10), 2753–2756 (October 1977).

[Sal13]   S. Sala, G. Zürn, T. Lompe, A. N. Wenz, S. Murmann, F. Serwane, S. Jochim, A. Saenz, *Coherent molecule formation in anharmonic potentials near confinement-induced resonances* (2013).

Bibliography

[Sch08] U. Schneider, L. Hackermüller, S. Will, T. Best, I. Bloch, T. Costi, R. Helmes, D. Rasch, A. Rosch, *Metallic and insulating phases of repulsively interacting fermions in a 3D optical lattice*, Science **322**(5907), 1520–1525 (2008).

[Sch10] U. Schneider, *Interacting Fermionic Atoms in Optical Lattices—A Quantum Simulator for Condensed Matter Physics*, Dissertation, Ph. D. Thesis, Johannes Gutenberg-Universität Mainz (2010).

[Ser07] F. Serwane, *The setup of a Magneto Optical Trap for the preparation of a mesoscopic degenerate Fermi gas*, Diploma thesis (2007).

[Ser11a] F. Serwane, *Deterministic preparation of a tunable few-fermion system*, Dissertation, Ruperto-Carola University of Heidelberg (2011).

[Ser11b] F. Serwane, G. Zürn, T. Lompe, T. B. Ottenstein, A. N. Wenz, S. Jochim, *Deterministic preparation of a tunable few-fermion system*, Science **332**(6027), 336–338 (2011).

[She10] J. F. Sherson, C. Weitenberg, M. Endres, M. Cheneau, I. Bloch, S. Kuhr, *Single-atom-resolved fluorescence imaging of an atomic Mott insulator*, Nature **467**(7311), 68–72 (2010).

[SK98] D. M. Stamper-Kurn, H.-J. Miesner, A. P. Chikkatur, S. Inouye, J. Stenger, W. Ketterle, *Reversible Formation of a Bose-Einstein Condensate*, Phys. Rev. Lett. **81**, 2194–2197 (Sep 1998).

[Sta00] R. Staudt, M. Dzierzawa, A. Muramatsu, *Phase diagram of the three-dimensional Hubbard model at half filling*, The European Physical Journal B-Condensed Matter and Complex Systems **17**(3), 411–415 (2000).

[Swe90] W. C. Sweatt, *Rotatable shear plate interferometer*, Optical Engineering **29**(9), 1157–1160 (1990).

[Tro08] S. Trotzky, P. Cheinet, S. Fölling, M. Feld, U. Schnorrberger, A. M. Rey, A. Polkovnikov, E. A. Demler, M. D. Lukin, I. Bloch1†, *Time-Resolved Observation and Control of Superexchange Interactions with Ultracold Atoms in Optical Lattices*, Science **319**, 295 (2008).

[Wen13] A. Wenz, G. Zürn, T. Lompe, S. Murmann, I. Brouzos, S. Jochim, *From few to many: Observing the Formation of a Fermi sea one atom at a time.*, in preparation (2013).

[Wer05] F. Werner, O. Parcollet, A. Georges, S. Hassan, *Interaction-induced adiabatic cooling and antiferromagnetism of cold fermions in optical lattices*, Physical review letters **95**(5), 056401 (2005).

[Yos96] K. Yosida, *Theory of Magnetism Springer: Series in Solid-State Sciences* (Berlin: Springer, 1996).

[Zü09]   G. Zürn, *Realization of an Optical Microtrap for a Highly Degenerate Fermi Gas*, Diploma thesis (2009).

[Zü12a] G. Zürn, *Few-fermion systems in one dimension*, Dissertation, Ruperto-Carola-University of Heidelberg (2012).

[Zü12b] G. Zürn, F. Serwane, T. Lompe, A. N. Wenz, M. G. Ries, J. E. Bohn, S. Jochim, *Fermionization of two distinguishable fermions*, Phys. Rev. Lett. (November 2012).

[Zü13]   G. Zürn, T. Lompe, A. N. Wenz, S. Jochim, P. S. Julienne, J. M. Hutson, *Precise Characterization of ^{6}Li Feshbach Resonances Using Trap-Sideband-Resolved RF Spectroscopy of Weakly Bound Molecules*, Phys. Rev. Lett. **110**, 135301 (Mar 2013).

Danksagung

An dieser Stelle möchte ich all jenen danken, die mich während meines Studiums und meiner Masterarbeit begleitet, motiviert und unterstützt haben.

Zunächst danke ich *Selim* dafür, dass er mich in seine Gruppe aufgenommen hat. Seine Begeisterung an der Physik hat mich bereits während des Studiums und meiner Zeit als HiWi in der Gruppe angesteckt. Die Entscheidung für eine Masterarbeit dort fiel mir deshalb nicht schwer. Für meine Fragen hat er sich immer geduldig Zeit genommen und nicht selten habe ich nach spannenden Diskussionen sein Büro völlig begeistert verlassen. Mit seinen fachlichen Tipps und Anregungen und vor allem auch mit seinem Vertrauen in mich hat er mich enorm motiviert.

Der Gruppe danke ich für die tolle Atmosphäre während der Arbeit, die witzigen Gespräche beim Mittagessen und die spannenden Tischkickerspiele. Dem guten Zusammenhalt in der Gruppe und dem Einsatz jedes einzelnen war es zu verdanken, dass der Umzug vom MPI-K zum neuen PI so reibungslos verlaufen ist; aber auch bei allen anderen Problemen und Hürden wird immer gemeinsam angepackt. Ich schätze mich glücklich Teil einer so tollen Gruppe zu sein.

Thomas danke ich für die interessanten Diskussionen und seine unermüdlich Geduld, mit der er meine teils konfusen Fragen zu Experiment und Theorie beantwortet. Seine Unterstützung bei der Laborarbeit und sein Ansporn haben wesentlich zum Gelingen dieser Arbeit beigetragen.

Gerhard danke ich für seine Expertise bezüglich der Feshbachspulen und der Mikrofalle und für die massiven, stabilen und zweckdienlichen G-Konstruktionen im Experiment.

Friedhelm, der das hochauflösende Objektiv designed hat, war am EMBL immer der Telephonjocker bei Fragen rund ums Objektiv. Er hat mir stets nützliche Tipps und Diagnosewerkzeuge wie das Shearplate zukommen lassen.

Zusammen mit *Vincent* hab ich den optischen Aufbau für die Mikrofalle charakterisiert. Seiner hervorragenden Vorarbeit ist die gute Performance des Aufbaus zu verdanken.

Bei *Simon* bedanke ich mich vor allem für die tolle Zusammenarbeit beim Einbau der neuen Mikrofalle. Geduldig hat er sich mit mir und Thomas die Nächte um die Ohren geschlagen um nach dem Umzug und dem Umbau das Experiment in Rekordzeit wieder in Betrieb zu nehmen. In ihm habe ich auch einen Seelenverwandten bezüglich Kaffee- und Kuchenkonsum gefunden.

André danke ich für seinen immerwährenden Optimismus, *Martin* für die netten Gespräche, die sich nicht um das lederne Rund drehten, *Puneet* für die englischen Wortwitze und die lustige Zeit im Büro, *Mathias* für die vielen Tipps bezüglich

Erklärung:

Ich versichere, dass ich diese Arbeit selbstständig verfasst habe und keine anderen als die angegebenen Quellen und Hilfsmittel benutzt habe.

Heidelberg, den (Datum)   . . . .